

Quantitative MALDI imaging of aspirin metabolites in mouse models of triple-negative breast cancer

Tae-Hun Hahm,^{a,b} Dalton R. Brown,^a Caitlin M. Tressler,^{a,b} Thao Tran,^c Alice Ly,^c Arvind P. Pathak,^{b,d,e} Michael T. McMahon,^{b,f} Kristine Glunde,^{*,a,b,e,g}

^a The Johns Hopkins Applied Imaging Mass Spectrometry Core and Service Center, Division of Cancer Imaging Research,

^b The Russell H. Morgan Department of Radiology and Radiological Science, The Johns Hopkins University School of Medicine, Baltimore, MD 21205, USA

^c Aspect Analytics NV, C-mine 12, 3600 Genk, Belgium

^d Department of Biomedical Engineering, The Johns Hopkins University School of Medicine, Baltimore, MD 21205, USA

^e The Sidney Kimmel Comprehensive Cancer Center, The Johns Hopkins University School of Medicine, Baltimore, MD 21205, USA Aspect

^f F.M. Kirby Research Center for Functional Brain Imaging, Kennedy Krieger Institute, Baltimore, MD 21205, USA

^g Department of Biological Chemistry, The Johns Hopkins University School of Medicine, Baltimore, MD 21205, USA

*Corresponding author. Email: kglunde1@jhmi.edu; Phone: (410) 614-2705; Fax: (410) 614-1948
Kristine Glunde, Ph.D.

Professor of Radiology, Oncology and Biological Chemistry

Director, Applied Imaging Mass Spectrometry (AIMS)

The Johns Hopkins University School of Medicine

Russell H. Morgan Department of Radiology and Radiological Science

Division of Cancer Imaging Research

720 Rutland Avenue

Traylor Building, Room 203

Baltimore, MD 21205

U.S.A.

email: kglunde@mri.jhu.edu

Lab website: <http://glundelab.org/>

Core website: www.hopkinsmedicine.org/radiology/aims

Abstract

Rationale: The non-steroidal anti-inflammatory drug aspirin is currently being developed as activatable contrast agent for chemical exchange saturation transfer (CEST) magnetic resonance imaging (MRI), for detection of its CEST MRI active metabolite salicylic acid (SA). This study refines and develops quantitative matrix-assisted laser desorption/ionization (QMALDI) imaging to investigate the distribution of aspirin metabolites including SA in triple-negative breast cancer (TNBC) models in mice.

Method: In this study, we established QMALDI imaging with norharmane (nH) matrix and assisted by the addition of 5 mM PAA for optimized SA detection. Deuterated D₆-SA was added as an internal standard to quantify SA detection. PAA was applied via spraying to improve matrix uniformity and reduce crystal size by forming hydrogen bonds with the nH matrix. Ultraviolet (UV) irradiation during MALDI imaging activated PAA, generating reactive radicals that facilitated the breakdown of nH matrix compounds, thereby reducing matrix-related noise.

Results: QMALDI imaging with 5 mM PAA-doped nH matrix and D₆-SA as internal standard revealed SA accumulation of 141.9 ± 22.6 pmol/mm² in the liver, 129.5 ± 7.8 pmol/mm² in the kidney, and 50.4 ± 3.0 pmol/mm² in TNBC tumors following intravenous injection of aspirin in mice. Precise spatial alignment, integration, and quantification of MALDI imaging, histology, and immunofluorescence images from CD31 staining for blood vessels allowed us to accurately evaluate the spatial distribution of SA in tissue regions enriched with blood vessels and in specific anatomical regions. This spatial data analysis revealed high SA accumulation in the kidney medulla, viable tumor rim containing CD31-stained blood vessels, and throughout the liver.

Conclusion: This newly developed QMALDI imaging approach for detecting aspirin metabolites demonstrated high SA accumulation in the kidney medulla and tumor rim containing blood vessels within viable tumor regions following systemic aspirin injection in mice, consistent with our previous study using aspirin-generated SA as activated contrast agent for CEST MRI. This approach enhances the spatial and tissue structural accuracy of quantitative analysis, reinforcing the potential of QMALDI imaging for investigating contrast agents, drug distributions, and metabolism in various tissues.

Keywords: aspirin, salicylic acid, MALDI, imaging, quantitative, metabolites

Introduction

Aspirin and its metabolite salicylic acid (SA) are both well-established inhibitors of cyclooxygenase 1 and 2 (COX-1 and COX-2), allowing their extensive utilization in treating inflammation by inhibiting prostaglandin synthesis [1]. Aspirin is widely used in medicine because of its anti-inflammatory [3], analgesic [4], anti-cancer [5], and antipyretic [6] properties, facilitating the treatment of cardiovascular conditions, stroke, arthritis, and its usage as a chemopreventive agent to prevent cancers, notably breast cancer [1-5]. Beyond its therapeutic use, recent studies have identified SA and other salicylates as outstanding contrast agents, particularly for cancer imaging [7-9], through their intramolecular hydrogen bonds which enable strong chemical exchange saturation transfer (CEST) magnetic resonance imaging (MRI) contrast [9-12]. As a result, there is renewed interest in the biodistribution of SA and related compounds.

Previously employed methods for measuring the biodistribution of aspirin include autoradiography and gamma scintigraphy which provide precise location information by using ^3H , $^{99\text{m}}\text{Tc}$ -labelled diethylenetriamine pentaacetate (DTPA), samarium-152 oxide, or other forms of radiolabeling [13-15]. However, these methods do not provide precise information about the types of metabolites present within tissue, which would be beneficial to know. For example, some side effects caused by aspirin including hearing loss, stomach bleeding, and Reye's syndrome have yet unknown biological mechanisms, which could be revealed if spatial metabolic details were available [16]. Furthermore, detoxification of aspirin is thought to occur through glycine conjugation although the literature on the route of this conjugation is limited. A comprehensive understanding of aspirin metabolism and the tissue-specific accumulation of its metabolites would allow for a better understanding of aspirin's side effects, its CEST MRI tumor contrast generation, and its detoxification [17]. While CEST MRI can reveal the presence of one or two aspirin metabolites including SA and 2,5-dihydroxybenzoic acid (2,5-DHB) [9], there is an emerging need for new methods which can detect and quantify the presence of all aspirin metabolites in tissue at microscopic spatial resolution.

Our current study utilizes matrix-assisted laser desorption/ionization (MALDI) mass spectrometry (MS) imaging to measure and spatially resolve tissue levels of SA, a metabolite of aspirin as well as a new CEST MRI contrast agent. MALDI imaging is particularly well-suited for the spatially resolved detection of drug metabolites, which inherently exhibit different molecular weights, thereby providing a detailed molecular profile [18]. Quantitative MALDI (QMALDI) imaging offers a powerful approach for visualizing and quantifying multiple drug metabolites [19-21]. This capability makes QMALDI imaging a valuable tool for drug and contrast agent development studies. In addition, our study introduces an improved matrix spraying technique and an advanced image integration process to enhance the accuracy

and precision of QMALDI tissue imaging in conjunction with microscopic slide scanning following histological staining, or immunofluorescence (IF) staining. Developing targeted QMALDI imaging can significantly enhance our understanding of the tissue biodistribution of various drugs, as demonstrated in previous studies [20,21].

The goal of this study was to develop a robust QMALDI imaging technique to investigate the distribution of aspirin metabolites, particularly SA as an activatable CEST MRI contrast agent [9], in organs and tumors from triple-negative breast cancer (TNBC) models in mice which were intravenously injected with aspirin. To investigate the spatial and structural context of the aspirin metabolite distribution in tissues, several microscopic imaging techniques were integrated with QMALDI imaging of SA, which include CD31 IF staining for visualizing vascular networks as well as hematoxylin and eosin (H-E) staining for assessing tissue architecture. The integration of these methodologies establishes a comprehensive framework for visualizing contrast agent distribution, drug metabolism, and tissue characteristics. This approach contributes to the development of enhanced therapeutic strategies and diagnostic applications.

Methods

Materials. Unless otherwise noted, all solvents and trifluoroacetic acid (TFA) were purchased from Sigma Aldrich (St. Louis, MO). Peracetic acid (PAA), norharmane (nH), aspirin, SA. salicyl acyl glucuronide (SAG), salicyl phenolic glucuronide (SPG), salicyluric acid (SU), 2,5-dihydroxybenzoic acid (2,5-DHB), D-mannitol, glycine, goat serum, Mayer's hematoxylin solution, and aqueous Eosin Y solution were purchased from Sigma-Aldrich (St. Louis, MO, USA). D₆-salicylic acid (D₆-SA), 4',6-diamidino-2-phenylindole (DAPI) solution and 4% paraformaldehyde (PFA) were purchased from Thermo Fisher (Waltham, MA). Citrate buffer was purchased from Biolegend (San Diego, CA). All solvents and reagents, which were of analytical grade, were employed without further purification.

Animal Study and Tissue Collection. All animal experiments were conducted following protocols approved by the Johns Hopkins University Institutional Animal Care and Use Committee (IACUC). All mice were housed under specific pathogen-free conditions in the Johns Hopkins University animal facility. Two million triple-negative human SUM159 breast cancer cells were inoculated into the right 4th mammary fat pad of 6–8-week-old female athymic nude mice (Envigo RMS LLC, Indianapolis, IN, USA). Tumor-bearing mice with tumor volumes ranging from 300 to 500 mm³ were administered with 100 μ L of injectable aspirin (aspirin DL-lysine) at concentrations of 0 mM or 300 mM into their tail veins. Their kidneys, livers, and SUM159 tumors were collected at 60 min following intravenous aspirin administration and frozen in liquid nitrogen vapors. Organs and tumors were stored at –80 °C until MALDI imaging experiments were performed.

Preparations of the Tissue Sections. Frozen SUM159 tumors, kidneys, and livers were cryo-sectioned into 20- μ m-thick sections on a CM1860 UV Cryostat (Leica Biosystems, Wetzlar, Germany) and thaw mounted onto pre-washed, poly-L-lysine coated indium tin oxide (ITO) slides (Delta Technologies, Loveland, CO). These tissue sections were used for quantitative MALDI imaging, as well as H-E and CD31 IF staining analyses, to evaluate and compare their spatial distribution characteristics. The sections were stored in vacuum-sealed slide mailers at –80 °C until matrix deposition. Prior to matrix application, the slides were equilibrated to ambient temperature by placing them in a vacuum desiccator. Norharmane (nH) matrix (10 mg/mL in 70% acetonitrile (ACN) with 0.1% TFA) was prepared with 5 mM peracetic acid (PAA) as an additive and 10 mM D₆-SA as an internal standard (IS). The solution was uniformly applied to the tissue sections on ITO slides using an HTX M3+ sprayer (HTX Technologies LLC, Chapel Hill, NC). The spraying parameters were set as follows: temperature at 70 °C, nozzle velocity at 1000 mm/min, flow rate at 100 μ L/min, with 20 passes and a track spacing of 2 mm. A drying time of 2 s was maintained between passes, and nitrogen gas was supplied at a pressure of 10 psi.

Polarized Light Microscopy. Polarized light microscopy images were acquired using an Olympus Slideview VS200 slide scanner (Evident, Waltham, MA, USA) with OlyVIA 4.1.1 software and a 40 \times

objective lens at the Johns Hopkins Applied Imaging Mass Spectrometry (AIMS) Core facility. Linear polarizers were precisely positioned at the front focal plane of the condenser and the rear focal plane of the objective lens. These polarizers were rotated to achieve optimal extinction, with a 95-degree setting used, enabling high-contrast visualization of birefringent materials, such as MALDI matrix crystals.

Scanning Electron Microscopy (SEM) Analysis. For SEM analysis, matrix-coated slides with varying concentrations of PAA were mounted on 51 mm holders using copper and carbon adhesive tapes. This ensured stable attachment of the samples and provided the necessary conductivity for electron microscopy. SEM imaging was performed using a JEOL JSM-IT700HR InTouchScope™ microscope (JEOL, Tokyo, Japan) at 3,000× magnification, with an accelerating voltage of 10 kV and a working distance of 13.5 mm. The analysis took place at the Materials Characterization & Processing (MCP) Core Facility. These imaging parameters were optimized to achieve high-resolution surface morphology of the matrix-coated samples, allowing for detailed observation of structural features.

QMALDI Imaging. The matrix-sprayed tissue sections were analyzed on a timsTOF fleX MALDI-2 mass spectrometer (Bruker Daltonics, Bremen, Germany) equipped with a dual ESI/MALDI source and a 10 kHz smartbeam 3D neodymium (Nd): yttrium Aluminum Garnet (YAG) laser operating at 355 nm for MALDI imaging at the Johns Hopkins Applied Imaging Mass Spectrometry (AIMS) Core facility. Prior to data acquisition, height adjustment (target profile generation) and laser focus tuning were performed. Mass calibration was conducted using electrospray ionization (ESI) of Agilent ESI-L Tune Mix, followed by calibration with red phosphorus to achieve a mass error of less than 1 ppm. MALDI parameters in qTOF mode were optimized to enhance signal intensity by adjusting ion optics, laser intensity, and laser focus. The MALDI acquisition settings included: MALDI plate offset of 50 V, deflection 1 delta of 70 V, funnel 1 RF of 350 Vpp, funnel 2 RF of 350 Vpp, multipole RF of 400 Vpp, collision cell energy of 10 eV, collision RF of 1800 Vpp, quadrupole ion energy of 5 eV with a low mass cutoff at m/z 50 Da, focus pre-TOF transfer time of 70 μ s, and prepulse storage time of 10 μ s. Imaging was performed over the m/z range of 20–900 Da in negative ion mode, with raster widths of 100 or 20 μ m and 600 shots per pixel at a laser frequency of 10 kHz. Tandem MS experiments were performed with nitrogen as collision gas, using a sum of 5 spectra with 1300 shots per pixel across the m/z range of 50–900 Da. The laser power was set to 90% with an isolation window of ± 1 Da and a collision energy of 30–40 eV. MALDI imaging data were imported into SCiLS Lab (version 2024b, Bruker Daltonics) for visualization and analysis, focusing on average spectra within the MS imaging region. Average intensity measurements were calculated in SCiLS Lab software by summing all spectra within each region of interest (ROI) and dividing by the total pixel count in that region (standardized at 100 pixels/mm²). Calibration curves were established by analyzing SA standard spots ranging from 2 to 300 pmol/0.2 μ L spot. For each standard concentration, circular ROIs (~2 mm² as measured by SCiLS Lab software) were drawn to encompass the entire dried droplet spot area. The ratio of SA signal intensity to D₆-SA (internal standard) intensity was

calculated for each concentration and plotted to generate the calibration curve. The weight of the tissue section (20 μm) was 343 μg /liver section, 356 μg /kidney section, and 450 μg /SUM159 tumor section. Tissue section areas were determined by pixel count analysis in SCiLS Lab software, equating to $48.84 \pm 1.66 \text{ mm}^2$ for liver sections (4884 ± 166 pixels), $44.03 \pm 0.63 \text{ mm}^2$ for kidney sections (4403 ± 63 pixels), and $34.76 \pm 0.76 \text{ mm}^2$ for SUM159 tumor sections (3476 ± 77 pixels). The final SA tissue concentration was expressed as pmol/mm^2 , calculated by applying the calibration curve equation to the measured SA/D₆-SA intensity ratios from each tissue section, enabling direct comparison of SA accumulation across different tissue types. Limits of detection (LOD) and quantification (LOQ) were calculated based on previously established equations [22]. Tandem MS spectra were processed and analyzed using dataAnalysis (version 5.3.236, Bruker Daltonics).

MALDI-MS Analysis for Validating the PAA Mechanism. Frozen tissue sections (liver, kidney, and SUM159 tumor) were prepared as described previously using 20- μm -thick cryosections mounted on ITO slides. Each tissue type was sectioned to provide three sequential sections for the three experimental conditions to ensure comparable tissue morphology across treatments. Matrix solutions were applied using an HTX M3+ sprayer under identical conditions: temperature at 70°C , nozzle velocity at 1000 mm/min, flow rate at 100 $\mu\text{L}/\text{min}$, with 20 passes and a track spacing of 2 mm. A drying time of 2 s was maintained between passes, and nitrogen gas was supplied at 10 psi pressure. Three matrix conditions were prepared to test the role of hydroxyl radicals in the PAA mechanism as follows. Control: nH matrix solution (10 mg/mL in 70% ACN with 0.1% TFA) without additives; PAA: nH matrix solution with 5 mM PAA; PAA + scavenger: nH matrix solution with 5 mM PAA and 100 mM D-mannitol. MALDI imaging was performed on a timsTOF fleX MALDI-2 mass spectrometer using identical acquisition parameters across all three conditions. Key analytical targets included the matrix background signals at m/z 154.97 and m/z 248.96 (nH matrix-derived ions), the hydroxyl radical scavenger D-mannitol at m/z 181.07 ($[\text{M}-\text{H}]^-$ ion of D-mannitol). Imaging parameters were set to 100 μm pixel size in negative ion mode, with 600 shots per pixel at 10 kHz laser frequency. MALDI imaging data were processed using SCiLS Lab software (version 2024b, Bruker Daltonics). ROI analysis was performed to observe signal intensities of matrix background ions (m/z 154.97 and 248.96) across the three experimental conditions. Average spectra were generated from equivalent tissue regions to compare signal intensity changes.

Immunofluorescence Staining and Microscopy. Following MALDI imaging, SUM159 tumor sections were immersed in 100% ethanol for a minimum of 24 h to remove the MALDI matrix. The sections were then rinsed with ethanol and fixed in freshly prepared 4% paraformaldehyde (PFA) at room temperature for 15 min. Post-fixation the tumor sections were incubated in a 10 mM citrate buffer (pH 6.0) followed by a 0.01 M phosphate-buffered saline (PBS, pH 7.2) wash. Subsequently, the sections were blocked in a solution containing 20% goat serum, 1% bovine serum albumin (BSA), 0.3 M glycine, and 0.01 M PBS

(pH 7.2) for 24 h at 4 °C. The sections were then incubated with a primary anti-CD31 antibody (1:20, R&D Systems, Minneapolis, MN) for 24 h at 4 °C. CD31 immunostaining was completed by incubating the sections with donkey anti-goat IgG (H+L) highly cross-adsorbed secondary antibody, Alexa Fluor™ Plus 647 (1:100, Invitrogen, Carlsbad, CA) at 37 °C for 3 h. Nuclei were stained with DAPI (1:1000) for 2 min, then washed with PBS for 5 min at 70 rpm shaking before mounting. Imaging of DAPI and CD31 to visualize mouse tumor vasculature was performed using an Olympus Slideview VS200 slide scanner equipped with OlyVIA 4.1.1 software and a 40× objective lens at the Johns Hopkins Applied Imaging Mass Spectrometry (AIMS) Core facility. The imaging was conducted with excitation wavelengths of 378/52 nm for DAPI (emission at 432/36 nm) and 635/18 nm for Alexa 647 (emission at 652/42 nm), respectively.

Histological Staining. Hematoxylin and eosin (H-E) staining was performed on the same sections used for MALDI imaging experiments. The residual matrix was removed by submerging slides in 100% ethanol (24 h). Slides were submerged in 70% ethanol for a second time (3 min), followed by Milli-Q water (3 min). Staining was performed in hematoxylin (3 min), followed by rinsing under running tap water (3 min), eosin (30 s), running tap water (1 min), 100% ethanol (1 min), and xylene (30 s). Optical images were acquired at 40× magnification using an Olympus Slideview VS200 slide scanner equipped with OlyVIA 4.1.1 software (Evident, Waltham, MA, USA).

Integrative Data Analysis Approach using the Weave Software. All the following image analysis steps were conducted using the new Weave Platform-Version v1.217.11 (Aspect Analytics NV, Genk, Belgium). The WEAVE software integrates MALDI-MS imaging (MSI) with various optical images by image co-registration and resampling of the MALDI-MSI pixels (20 µm/pixel) with nearest neighbor interpolation to exactly match the dimension and pixel spacing of immunofluorescence (IF) and H-E microscopy images (0.325 µm/pixel). In effect, this means there are multiple IF or H-E pixels underneath each MSI pixel after transformation. Mean value aggregation of multiple IF or H-E pixels that are underneath a single MSI pixel is then possible.

For preprocessing, raw MALDI imaging data were converted to imzML format for further processing. The imaging data underwent preprocessing with total ion current (TIC) normalization to standardize signal intensities across all spectra. We selected peaks corresponding to SA, defined by their respective m/z values of 137.0247 Da. To ensure accurate peak detection, intensities were aggregated using a tolerance window of ± 0.05 Da around these m/z values. The binned intensities were then utilized for generating ion images, facilitating subsequent data integration and visualization.

For integrating microscopic imaging modalities, H-E, MALDI, and IF images were manually co-registered using non-rigid registration [23]. To align the MALDI imaging data with the corresponding H-E image, ion images of SA were utilized directly to identify landmarks for the non-rigid image co-

registration. Similarly, the IF image was co-registered to the H-E image using the same manual non-rigid workflow in the Weave Platform. Finally, both MALDI ion images and IF images were transformed into the spatial coordinate system of the corresponding H-E images.

After aligning the MALDI ion and IF images, IF image pixels (0.325 $\mu\text{m}/\text{pixel}$) were down sampled to the resolution of the MALDI ion image pixel masks (20 $\mu\text{m}/\text{pixel}$) for the calculation of mean IF intensity values per MALDI ion image pixel. This approach allowed us to perform quantitative comparisons of MALDI ion image signals in regions with varying levels of fluorescence staining intensity.

The resulting integrated dataset, comprising MALDI ion image intensities and mean IF intensities for each MALDI ion image pixel, enabled further analysis and extraction of MALDI ion image signal intensities based on fluorescence intensity thresholds in the CD31 stained IF image. Finally, the fused H-E, MALDI-MSI, and IF imaging data stacks were visualized using reports generated in the Weave Platform.

For tumor and kidney tissues, H-E-stained images with annotated regions were co-registered with MALDI images of SA using SCiLS Lab software. The normalized SA intensity was calculated for each defined region from these co-registered images. This assessment was conducted by measuring the SA intensity per pixel across all samples, and data visualization with violin plots was accomplished in R (version 4.4.3) using multiple graphical packages including lattice, plot3D, vioplot, and RColorBrewer. The comparative analysis was presented as an enhanced 3D violin plot incorporating multiple layers of visual information.

Statistical Analysis. Statistical analysis was implemented in R (version 4.4.3) utilizing packages including dplyr and base R statistical functions. Raw data were imported from a CSV file containing normalized SA intensity values for two regions. Following data preprocessing to remove "Not Applicable" values, descriptive statistics (median, mean, minimum, maximum, first and third quartiles, and standard deviation) were calculated for each tissue region. To determine if pixel-wise intensity distributions were significantly different between two ROIs from the same tissue section, a two-tailed Student's t-test was performed using R (version 4.4.3) and JSAP 0.19.3 (JSAP Software, Netherlands).

Results and Discussion

Peracetic Acid as Spray Additive for MALDI Tissue Imaging of Aspirin Metabolites

When optimizing MALDI matrices for qualitative and quantitative MALDI imaging, the interference caused by noise signals originating from matrix, metals, and other impurities in the tissue sample during the MALDI desorption and ionization process poses a challenge [24]. This is particularly relevant for aspirin metabolites because there is overlap between matrix ions and aspirin metabolites in the low mass range (m/z 0-500 Da) [21]. These noise signals can obscure the signals of interest, making it difficult to obtain a clear and accurate profile of drug distribution and metabolism. Therefore, removing matrix noise is an essential procedure and challenge for both qualitative and quantitative MALDI imaging analysis. In this study, we employed the nH matrix, which was previously used for detecting SA at m/z 137.02 Da in negative ion mode by MALDI profiling analysis [9]. Additionally, in this study, we tested for the first time the addition of low concentration peracetic acid (PAA) to nH matrix to further enhance the MALDI imaging data, which capitalizes on PAAs ability to generate reactive radicals when exposed to ultraviolet (UV) light. Upon UV irradiation, the bond between oxygen atoms in PAA breaks, forming reactive species as follows: $\text{CH}_3\text{CO}_3\text{H} \xrightarrow{h\nu} \text{CH}_3\text{CO}_2^\bullet + \bullet\text{OH}$ [25,26]. We hypothesized that the generation of these radicals will enhance PAA's oxidative reactivity during MALDI imaging, which uses UV light from a focused laser beam (e.g., a Nd: YAG laser at 355 nm), to break down nH matrix-related ions and remove matrix noise, as the nH matrix has a similar chemical structure as diclofenac and carbamazepine, which are reportedly broken down by PAA [27].

To investigate changes in SA intensity in MALDI imaging, 1 mM SA was applied as dried droplets on tissue sections from control mice (not treated with aspirin) prior to spraying the tissues with nH matrix. Then, nH matrix was sprayed onto these tissue sections with varying concentrations of PAA (0, 1, 5, 10, and 20 mM) as an additive. An increase in SA intensity was observed when adding 1 mM PAA as compared to control (0 mM PAA) (Figure 1 and Table 1). Furthermore, the SA intensity in tissue sections sprayed with nH with the addition of 5 mM PAA showed a substantial increase across various tissues, including liver, kidney, and SUM159 tumor, however, no significant changes in SA intensity were detected at higher PAA concentrations (10 mM and 20 mM). This effect was particularly pronounced in liver tissue, where a more than three-fold increase in the average SA signal intensity was observed, resulting in a significant enhancement in SA detection with 5 mM PAA as spray additive. Furthermore, to address concerns regarding the fragmentation of SA and its potential degradation by 5 mM PAA, we conducted a targeted analysis focusing on the known SA fragment ion at m/z 93.03 Da. As demonstrated in Figure S1, this specific ion was not detected in dried droplet samples on tissue sections following PAA application. The absence of this fragment provides strong evidence that SA remains stable under our experimental

conditions, with no significant degradation occurring due to PAA treatment.

There were additional benefits as well. At a concentration of 5 mM PAA, the PAA and nH matrix demonstrated a more uniform distribution of co-crystals, as observed in polarization images taken at 40× magnification, compared to samples sprayed with other PAA concentrations (Figures 1B and 1C). The SEM images of the nH matrix crystals with 5 mM PAA revealed significantly thinner and smaller crystal sizes ($0.64 \pm 0.05 \mu\text{m}^2$) than those formed at 0, 1, 10, and 20 mM PAA concentrations on tissue sections. The increased crystal uniformity and smaller crystal sizes achieved with 5 mM PAA are crucial for ensuring reproducible matrix application, which is essential for QMALDI imaging analysis [20]. As previously reported, hydrogen bonding interactions between the MALDI matrix and additives could lead to the formation of compact crystal structures [20]. Strong N–H \cdots O hydrogen bonds contribute to tighter packing and reduced matrix crystal size [28,29]. The concentration of the additive plays a crucial role in co-crystallization, affecting both crystal size and uniformity, which is essential for achieving reproducible and effective MALDI analysis [20,30]. In this study, the nitrogen atom in the pyridine ring of the nH matrix acts as a hydrogen bond donor, while the carbonyl oxygen (C=O) from PAA serves as a hydrogen bond acceptor. Consequently, hydrogen bonds can form between the carbonyl group of PAA and the N–H group from the nH matrix. The optimal concentration for co-crystallization with the nH matrix was identified as 5 mM PAA (Figure 1), resulting in smaller, evenly distributed crystals which help prevent inhomogeneities and reduce the risk of analyte delocalization, a common issue associated with larger crystals that can lower the resolution of MALDI-MSI [30,31]. When the PAA concentration exceeded 10 mM, crystal formation on tissue became less consistent, resulting in larger crystals compared to those formed off-tissue, which negatively impacted the signal intensity of SA in MALDI imaging.

The addition of 5 mM PAA in the spray enhanced the signal intensity of SA in the tissues of SUM159 tumors, livers, and kidneys of aspirin-treated mice without causing SA delocalization, while reducing noise signals from the matrix both on and off tissue (Figures S2, S3, and S4). Notably, MALDI images showed high background noise signals at m/z 154.97 Da and m/z 248.96 Da, which were significantly reduced after spraying of nH with 5 mM PAA as additive. The background signals at m/z 154.97 Da and m/z 248.96 Da were identified as originating from the nH matrix, rather than from endogenous tissue components (Figures S5 and S6). This was confirmed by comparing the fragmentation patterns of m/z 154.97 Da and m/z 248.96 Da between dried nH droplets and tissue sections from liver, kidney, and SUM159 tumor samples using tandem mass spectrometry. To directly validate our proposed mechanism that PAA reduces matrix background through MALDI imaging UV laser-induced hydroxyl radical generation, we conducted radical scavenging experiments using D-mannitol as a specific hydroxyl radical scavenger [32]. Three experimental conditions were compared: Control (nH matrix only), PAA (nH matrix + 5 mM PAA), and PAA + scavenger (nH matrix + 5 mM PAA + 100 mM D-mannitol) (Figure S7).

MALDI imaging analysis of matrix background signals demonstrated clear evidence supporting the hydroxyl radical mechanism. The characteristic nH matrix-derived ions at m/z 154.97 (Figure S7B) and m/z 248.96 (Figure S7C) showed reduced signal intensity following addition of PAA compared to control, and importantly, restoration of signal intensity was observed with PAA + scavenger where D-mannitol (Figure S7D) was present. This signal restoration was observed consistently across liver, kidney, and SUM159 tumor tissues. The combined effects of the MALDI imaging UV laser in conjunction with 5 mM PAA additive sprayed together with the nH matrix effectively reduced matrix noise signals without compromising the ionization of SA, the primary drug metabolite in this study.

Overall, the addition of 5 mM PAA significantly enhanced the SA peak intensity across all tested tissues. Compared to controls without PAA, we observed fold increases of 3.2 in liver, 1.8 in kidney, and 1.7 in SUM159 tumor tissues, resulting in a significant improvement in MALDI imaging of SA. The PAA spray additive for nH matrix deposition also improved matrix uniformity and led to a reduction in matrix crystal size, likely due to hydrogen bonding between PAA and nH matrix. However, when the concentration of PAA was increased to greater than 10 mM, both the matrix and dried SA droplets on the tissue underwent degradation, resulting in a decrease in SA intensity (Figure 1 and table 1). This high PAA concentration also led to the formation of larger, uneven crystals on the tissue, which likely interfered with MALDI imaging [20,30,31]. Therefore, our study clearly supports maintaining the PAA concentration at 5 mM to avoid these undesirable effects.

PAA-Assisted MALDI Imaging of the Distribution of Aspirin Metabolites in Various Tissues Sections

Next, we used this new approach to study the aspirin and SA distributions within various tissues. The structures and masses of aspirin, SA, and several other aspirin metabolites are shown in Figure 2. We examined the spatial distribution of the CEST MRI contrast active metabolite SA in tissues from mice growing SUM159 TNBC xenografts in their mammary fat pads, which were systemically injected into their tail veins with 300 mM aspirin and compared these mice to untreated control mice. SA was detected in the liver, kidney, and tumor tissues from SUM159 TNBC bearing mice treated with 300 mM aspirin but not in tissues from untreated control mice (Figure 3). To further validate the detection of SA in tissue sections following aspirin treatment, MALDI imaging was coupled with on-tissue tandem mass spectrometry. This analysis successfully identified a diagnostic SA fragment ion at m/z 93.03 Da, which was generated by fragmenting the molecular SA ion of $[M-H]^-$ at m/z 137.02 Da, confirming the presence of SA in TNBC tumors, as well as in livers and kidneys from aspirin-injected mice (Figure S13). Aspirin was identified in the kidneys as well, confirmed by the detection of its diagnostic fragment ion at m/z 137.03 Da from fragmenting the molecular aspirin ion of $[M-H]^-$ at m/z 179.03 Da (Figures S8 and S14). While there was a small peak detected at m/z 179.03 Da in the aspirin-treated livers, it was not significantly

above the background that was detected in treated control mice. Additionally, 2,5-DHB was detected in TNBC tumors, as well as in liver and kidney tissues. The identification of 2,5-DHB was supported by the diagnostic fragment ion at m/z 109.03 Da, which was generated by fragmenting the molecular 2,5-DHB ion of $[M-H]^-$ at m/z 153.02 Da (Figures S9 and S15). However, salicyl acyl glucuronide (SAG) at m/z 312.04 Da, salicyl phenolic glucuronide (SPG) at m/z 311.04 Da, and salicyluric acid (SU) at m/z 193.03 Da were not detected in any of the tissues analyzed, as illustrated in Figures S10, S11, and S12. This may result from low tissue metabolite levels of SAG, SPG, and SU below the detection threshold of MALDI imaging, a reduced ionization efficiency of SAG, SPG, and SU with MALDI, or more rapid breakdown, or less tissue accumulation of SAG, SPG, and SU as compared to aspirin, SA, and 2,5-DHB. Taken together, these results provide valuable information on the spatial distribution of several aspirin metabolites in various tissues and will allow us to further investigate and deepen our knowledge of the use of aspirin in cancer therapy and imaging.

QMALDI Imaging of SA in Tissue Sections with PAA Spray Additive and Deuterated Internal Standard

We further developed QMALDI imaging of SA by using PAA-assisted spraying of nH matrix and deuterated SA (D_6 -SA) as internal concentration standard to allow us to measure the absolute amount of SA in various tissues. Previous studies have demonstrated that the use of an internal standard is critical for accurate quantification in QMALDI imaging as it compensates for potential variability in ionization efficiency across different tissue types and tissue regions [20,33]. This is necessary because MALDI imaging can be affected by tissue composition, potentially leading to variations in signal intensity for the same analyte in different tissues and tissue regions because of differences in the molecular environment and local ion suppression [20,33,34]. By incorporating a deuterated internal standard, such tissue regional variations can be effectively normalized for [33], allowing for reliable and reproducible quantification of the target analyte across different tissue sections and regions.

Following this quantification approach (Figure S16), the MALDI images in Figures 4A show our calibration curves from dried droplet spots containing various SA concentrations on liver, kidney, and SUM159 tumor sections. Figure 4B shows the resulting linear correlations between the relative signal intensities of SA dried droplets (ranging from 1 to 150 pmol/mm²) normalized to D_6 -SA in liver ($R^2 = 0.9919$), kidney ($R^2 = 0.997$), and SUM159 TNBC tumor ($R^2 = 0.9951$) tissue sections prepared with 5 mM PAA, D_6 -SA, and nH matrix. Figure 4C demonstrates the uniform spatial distribution of D_6 -SA, which is used as a deuterated internal standard, across liver, kidney, and SUM159 TNBC tumor tissue sections following the application of the D_6 -SA spray, visualized by MALDI imaging. D_6 -SA was selected as the internal standard due to the enhanced stability of deuterated compounds under oxidative conditions compared to their non-deuterated counterparts [35,36]. The use of D_6 -SA enabled the normalization of

both SA intensity and its spatial distribution within the tissue sections, as shown in Figures 4A, 4C, and S17. This approach effectively compensated for variations in ionization efficiency across different tissue types and regions, allowing for quantitative comparison of ion images on an SA/D₆-SA intensity ratio scale, thereby ensuring accurate and reliable quantification of SA.

SA concentrations were quantitatively measured in liver, kidney, and SUM159 TNBC tumor tissues using three technical replicates per tissue type, where QMALDI imaging measurements were averaged from three directly adjacent tissues to enhance accuracy. The resulting SA tissue concentrations were 141.9 ± 22.6 pmol/mm² in the liver, 129.5 ± 7.8 pmol/mm² in the kidney, and 50.4 ± 3.0 pmol/mm² in the SUM159 TNBC tumor for three technical replicates per tissue type (Table 2). Additionally, biological replicates with three tissue samples each from three different mice were measured (Figures 6A, 7A, and S18) and showed an SA tissue concentration of 133.0 ± 44.6 pmol/mm² in the liver, 140.3 ± 23.3 pmol/mm² in the kidney, and 34.5 ± 10.8 pmol/mm² in the SUM159 TNBC tumor as quantified from three biological replicates each (Table 2). These results demonstrate that liver and kidney tissues contained higher SA tissue concentrations than SUM159 TNBC tumors.

Aspirin is known to rapidly hydrolyze into salicylic acid (SA) once it enters the body [37,38]. Therefore, it is not surprising that SA was detected and quantified in all tissues at 60 minutes following administration in this study. When aspirin is taken orally, it passes through the stomach wall and is metabolized in the liver before reaching other tissues [37]. However, in our experiments, we used intravenous administration, which allowed aspirin to directly enter the bloodstream, bypassing the stomach and liver, resulting in faster delivery to the tumor compared to oral administration. This likely minimized conversion into various metabolites, enabling more of the drug to reach the target organs and tumor. At 60 minutes post-injection, it is possible that SA concentrations had already peaked in various organs and entered the excretion phase, or that different tissues accumulated SA at different rates. However, since this study only analyzed tissues at the 60-minute time point, we could not observe concentration changes over time or measure SA levels in the blood. Future studies incorporating time-dependent tissue sampling and blood concentration analysis will be essential for a more comprehensive understanding of SA's spatial distribution and pharmacokinetics. Additionally, we observed larger standard deviations in SA tissue concentration between biological repeats compared to technical replicates (Table 2), which shows that the biological variability was larger than the technical variability. The high consistency observed between technical as well as biological replicates reinforces the reliability of the newly developed QMALDI imaging technique for detecting the spatial distribution and absolute quantitation of SA in tissue sections. These findings demonstrate that this technique provides accurate, quantitative spatial analysis of SA distributions in various tissue sections, highlighting its capability as a robust approach for studying drug metabolites in complex tissue samples.

Integrated Spatial Analysis of QMALDI SA Imaging with H-E Staining of Tissue Architecture and CD31 Immunofluorescence Staining of Vasculature

We were also interested in the biodistribution of SA with respect to tissue architecture and vasculature. To this extend, we performed H-E staining to evaluate anatomical tissue structures and CD31 IF staining to visualize vascular networks. We fused these imaging datasets, i.e., H-E, DAPI and CD31 IF, and MALDI imaging, as illustrated in Figure 5 and further analyzed the fused datasets. This was achieved by co-registering and scaling the MALDI images and CD31 and DAPI fluorescence images to the same pixel size which fused their spatial and intensity information. The higher resolution IF images were downsampled to the same resolution as the co-registered MALDI images, while ensuring that the corresponding pixels from different images were spatially matched. As a result, each pixel contained both the MALDI imaging information of SA abundance and the CD31 and DAPI fluorescence intensity (Figure 6A). We further analyzed and compared the SA intensity per pixel in areas classified as highly *versus* lowly vascularized regions based on their CD31 fluorescence intensity (Figure 6B). In all three biological replicates, SA levels were significantly higher in highly vascularized CD31-positive regions as compared to lowly vascularized CD31-negative regions. Additionally, H-E staining combined with MALDI imaging analysis consistently revealed higher SA levels in viable tumor regions compared to necrotic areas. This difference was also statistically significant across all three biological replicates (Figure 6C). Overall, our data demonstrates that SA predominantly accumulated in highly vascularized CD31-positive regions of viable tumor tissue.

We next evaluated the spatial distribution of SA abundance within kidney tissues and analyzed the fused data of MALDI imaging combined with H-E staining (Figure 7A). H-E-stained kidney tissue sections were annotated as medulla regions outlined with a yellow line and cortex regions outline with a blue line. Only regions with definitive anatomy were outlined. Our results revealed that higher levels of SA were detected in the medulla region than in the cortex region at the time of animal sacrifice, which was 60 minutes post-injection (Figure 7B). We therefore conclude that SA accumulated in the medulla region of kidneys at 60 minutes post-injection.

These QMALDI imaging findings are in good agreement with our previous CEST MRI study [9]. The spatial distribution of high SA levels in the kidney medulla and in the SUM159 tumor rim, which was CD31-positive and viable, as determined by QMALDI imaging in this study (Figure 6 and 7) is consistent with the SA distribution patterns we previously observed using SA CEST MRI [9]. Also, we observed a much higher signal contrast in kidney tissue than tumor tissue here, i.e., about 4 times higher, which is comparable to that observed by CEST MRI in our recent study. The QMALDI SA imaging approach developed in this study allows for a precise assessment of the spatial distribution of SA within organs and tumors, enabling researchers to evaluate their biodistribution at the microscopic level. The presented

approach of analyzing QMALDI imaging data combined with fused H-E and IF data from the same or directly adjacent tissue sections, will significantly enhance biological studies of the biodistribution of contrast agents, chemotherapy agents, and anti-inflammatory drugs [4-9].

Conclusions

We established a robust quantitative approach for targeted QMALDI imaging of SA by using nH matrix with 5 mM PAA as an additive and D₆-SA as a deuterated internal standard. While previous studies have explored various approaches for quantitative MALDI imaging, including isotopically labeled internal standards [39] and fluorescence-assisted matrix application [20], the current work introduces several novel elements that significantly advance the field. First, we demonstrate that PAA at 5 mM concentration serves as a unique dual-function additive that both enhances signal intensity and reduces matrix noise through PAA-generated radicals from UV light exposure by the MALDI imaging laser. The PAA-mediated hydrogen bonding with nH matrix generates exceptionally uniform, small crystal structures ($0.64 \pm 0.05 \mu\text{m}^2$), significantly enhancing both ionization efficiency and analytical reproducibility. This optimized microcrystalline morphology is critical for achieving consistent analyte desorption/ionization across tissue sections. This PAA-assisted MALDI imaging technique allows for precise quantification of SA, an aspirin metabolite and active CEST MRI contrast agent, while accurately mapping its spatial distribution in heterogeneous biological tissues.

This new QMALDI imaging technique was applied to quantitatively measuring SA in liver, kidney, and SUM159 TNBC tumor tissues in mice at 60 minutes following intravenous injection of aspirin. QMALDI imaging was able to quantify SA tissue concentrations of $133.0 \pm 44.6 \text{ pmol/mm}^2$ in the liver, $140.3 \pm 23.3 \text{ pmol/mm}^2$ in the kidney, and $34.5 \pm 10.8 \text{ pmol/mm}^2$ in the SUM159 TNBC tumor from three biological replicates each. High consistency observed between technical and biological replicates in this study reinforces the reliability of the newly developed QMALDI imaging technique for detecting the spatial distribution and absolute quantitation of SA in tissue sections.

Furthermore, we observed high SA in the kidney medulla and the CD31-positive, highly vascularized and viable regions in the tumor rim. This was possible by co-registration, scaling, and pixel matching of the MALDI imaging data with H-E stained, and CD31 and DAPI IF stained slide-scanned images of the same and adjacent tissue sections. These findings match our earlier findings with SA CEST MRI [9]. Targeted QMALDI SA imaging, as well as other similar QMALDI imaging approaches, allows us to accurately assess the spatial distribution and absolute concentration of drugs, drug metabolites, and contrast agents in various tissues for advancing our understanding of their biodistribution and biomedical effects, as well as helping to eventually move these approaches into clinical applications.

Tables

Table 1. Impact of PAA concentration on average spectra of dried SA droplets

Mode	Analyte	Tissue Type	0 mM PAA (SA intensity) ^a	1 mM PAA (SA intensity) ^a	5 mM PAA (SA intensity) ^a	10 mM PAA (SA intensity) ^a	20 mM PAA (SA intensity) ^a
Negative	SA	Liver	48.9 ± 18.6	66.5 ± 42.3	157.3 ± 26.2	37.7 ± 15.1	21.7 ± 24.5
		Kidney	379.4 ± 125.3	335.3 ± 57.7	692.3 ± 165.2	121.1 ± 21.3	42.1 ± 22.3
		SUM159	333.7 ± 42.5	424.0 ± 78.1	550.4 ± 24.1	164.8 ± 17.3	267.7 ± 23.1

^a: n = 3

Table 2. QMALDI imaging analysis of SA in various tissues

Mode	Analyte	Tissue Type	LOD (pmol/mm ²)	LOQ (pmol/mm ²)	Technical Repeats (pmol/mm ²) ^a	Biological Repeats (pmol/mm ²) ^a
Negative	SA	Liver	0.3	0.9	141.9 ± 22.6	133.0 ± 44.6
		Kidney	0.2	0.6	129.5 ± 7.8	140.3 ± 23.3
		SUM159	0.4	1.3	50.4 ± 3.0	34.5 ± 10.8

^a: n = 3

Figures

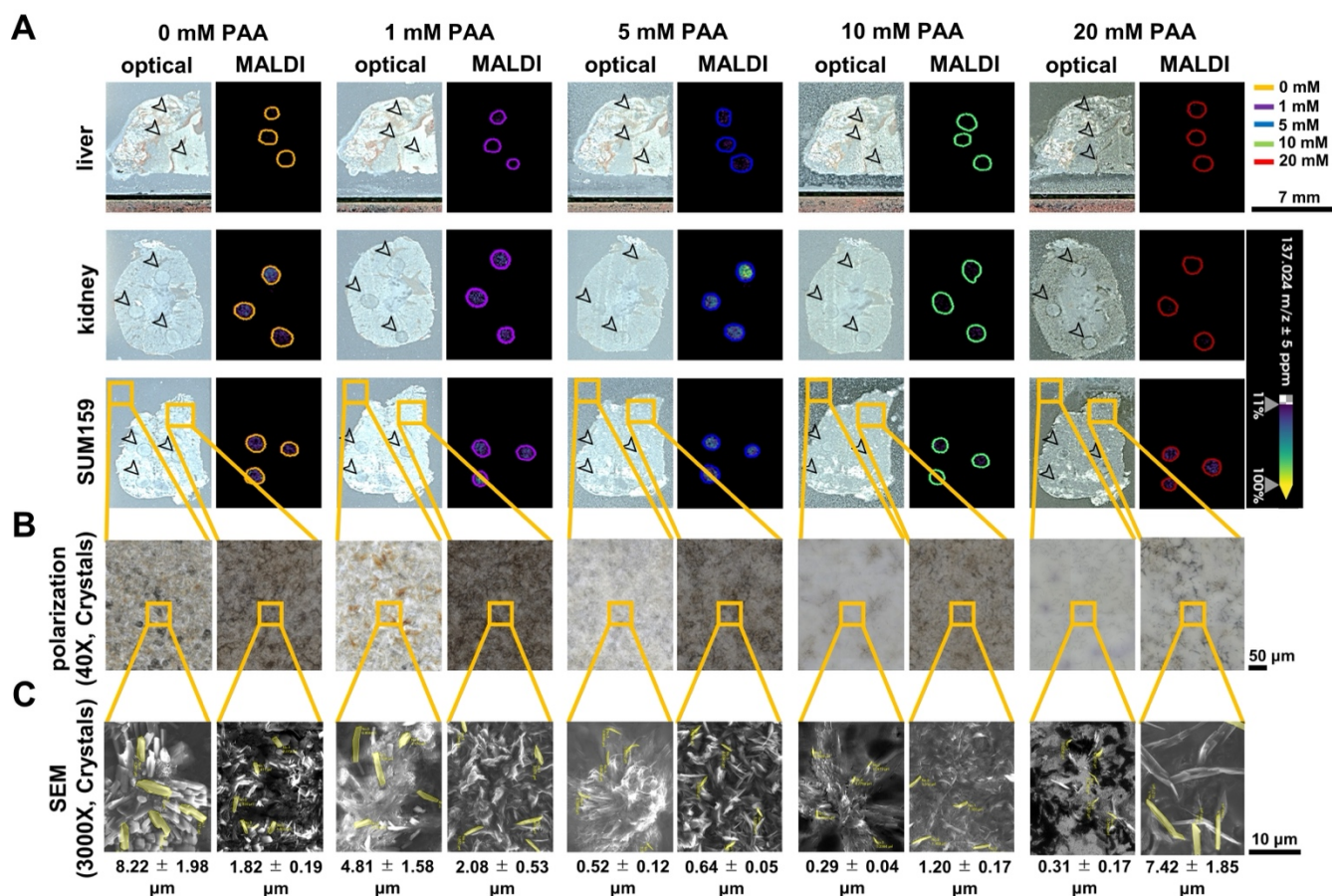


Figure 1. Effect of PAA concentration on SA detection in tissue samples. (A) Optical and MALDI images of tissue sections spotted with dried droplets of 1 mM salicylic acid (SA) prior to application of norharmane (nH), combined with varying concentrations of peracetic acid (PAA) (0 mM, 1 mM, 5 mM, 10 mM, and 20 mM). Black arrows indicate the locations of the dried SA droplets in the optical images. (B) Polarized light microscopy (40 \times) and scanning electron microscopy (SEM, 3000 \times) images were taken from the orange square-marked region shown in panel A. Matrix-Assisted Laser Desorption/Ionization (MALDI) images were acquired at a 100 μm pixel resolution in negative ion mode using a timsTOF fleX MALDI-2 instrument. The data highlight the detection of the $[\text{M}-\text{H}]^-$ ion of SA at m/z 137.02 Da in dried droplets spotted onto tissue sections. The average SEM crystal size was determined from five randomly selected crystals (highlighted in yellow) in each image and is presented as the mean \pm standard deviation (SD).

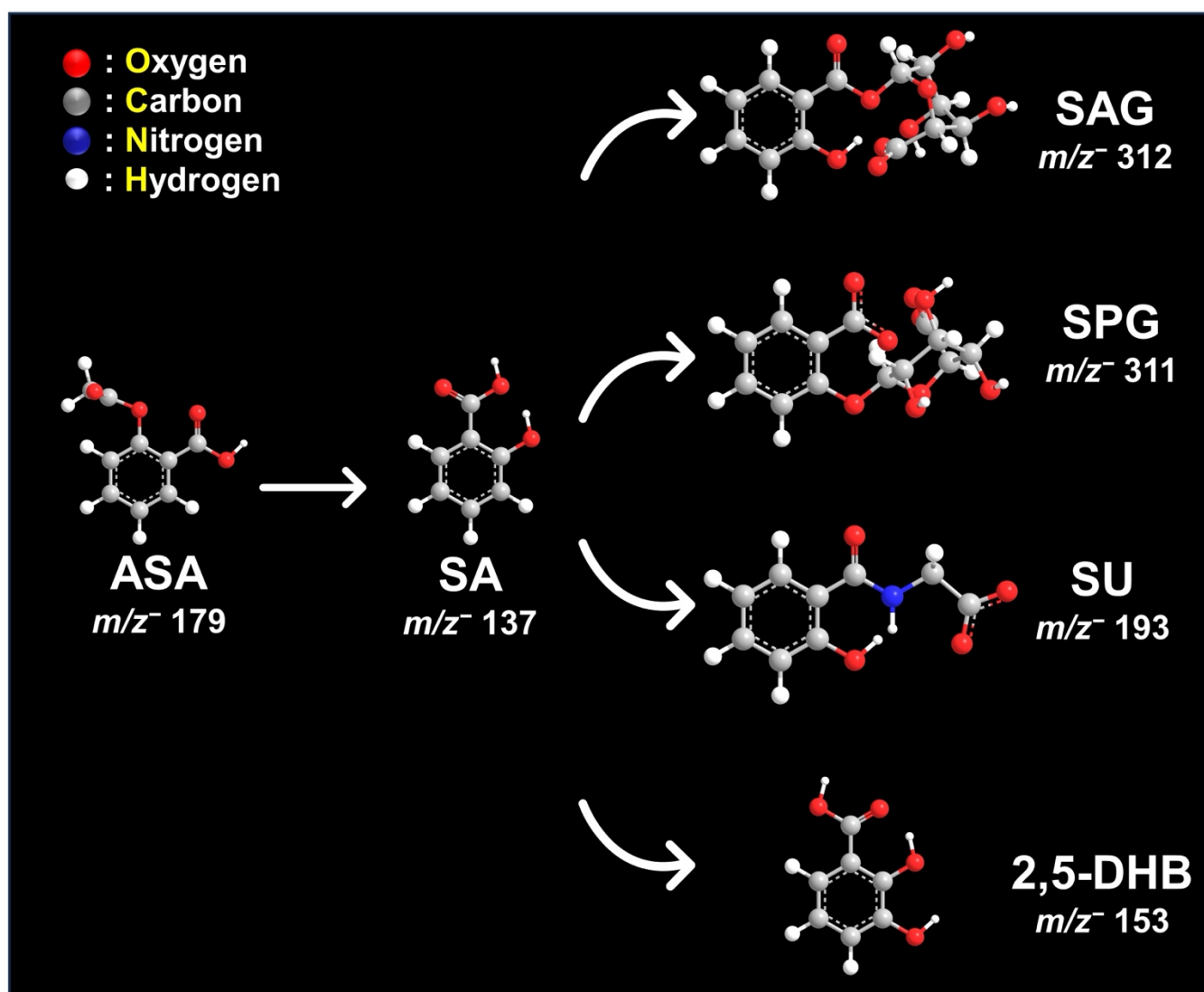


Figure 2. Schematic Representation of aspirin metabolites. Chemical structures and m/z values in negative ion mode for aspirin (ASA), salicylic acid (SA), salicyl acyl glucuronide (SAG), salicyl phenolic glucuronide (SPG), salicyluric acid (SU), and 2,5-dihydroxybenzoic acid (2,5-DHB).

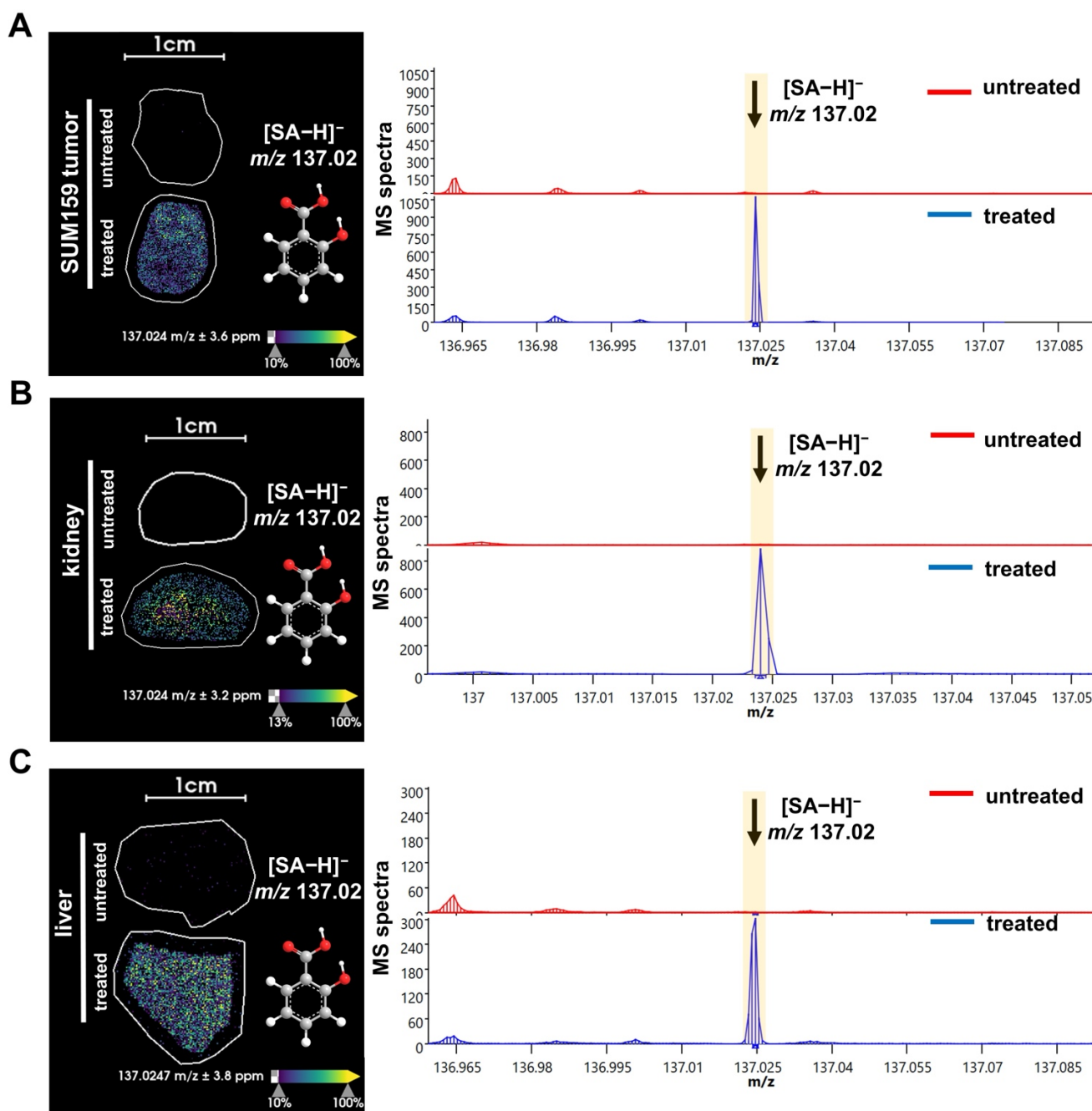


Figure 3. MALDI imaging of SA distribution in tissues from aspirin treated versus untreated mice. MALDI images and corresponding average spectra of SA distribution in (A) liver, (B) kidney, and (C) orthotopic SUM159 tumor xenograft of representative central tissue sections obtained from untreated control mice (top, red spectra) versus treated, 300 mM aspirin-injected mice (bottom, blue spectra). The data clearly show that the [M-H]⁻ ion of SA at m/z 137.02 Da is detected in tissue sections from treated mice, while it is absent in tissues from untreated mice. The MALDI images were acquired at 100 μ m pixel size in negative ion mode using a timsTOF fleX MALDI-2 instrument using norharmane matrix and peracetic acid additive.

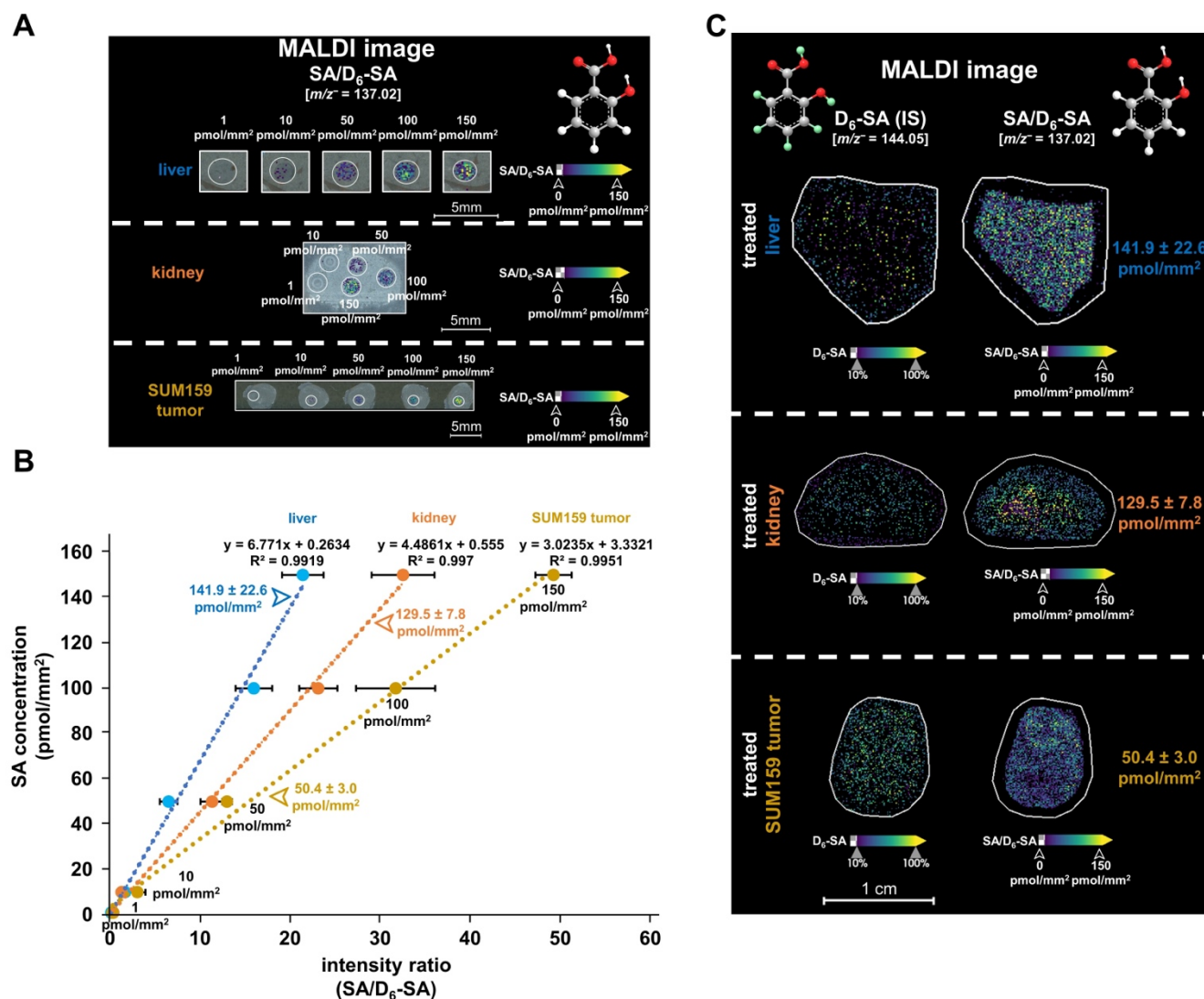


Figure 4. Quantification of SA in liver, kidney, and SUM159 tumor tissue sections. (A) MALDI images of salicylic acid dried droplets (SA, [*M*-H]⁻, *m/z* 137.02 Da, 0.5–150 pmol/mm²) were spotted onto untreated tissue sections, measured by QMALDI imaging in negative ion mode, and are shown as normalized SA images of the SA-to-D₆-SA ratio. (B) Calibration curves of SA were generated using QMALDI imaging in negative ion mode with D₆-SA as deuterated internal standard and peracetic acid as additive. SA-to-D₆-SA intensity ratios to generated calibration curves. MS intensities were derived from the average spectra of each circled SA dried droplet spot for each SA concentration as shown in panel A. (C) MALDI images of D₆-SA and normalized images of SA-to-D₆-SA ratio were acquired and are shown from data analysis in SCLIS lab. The measured concentrations of SA in the liver, kidney, and SUM159 tumor tissues of mice injected with 300 mM aspirin were 141.9 ± 22.6 pmol/mm², 129.5 ± 7.8 pmol/mm², and 50.4 ± 3.0 pmol/mm², respectively, as shown in panels B and C. The results are presented as mean \pm SD from three independent technical replicates of tissues.

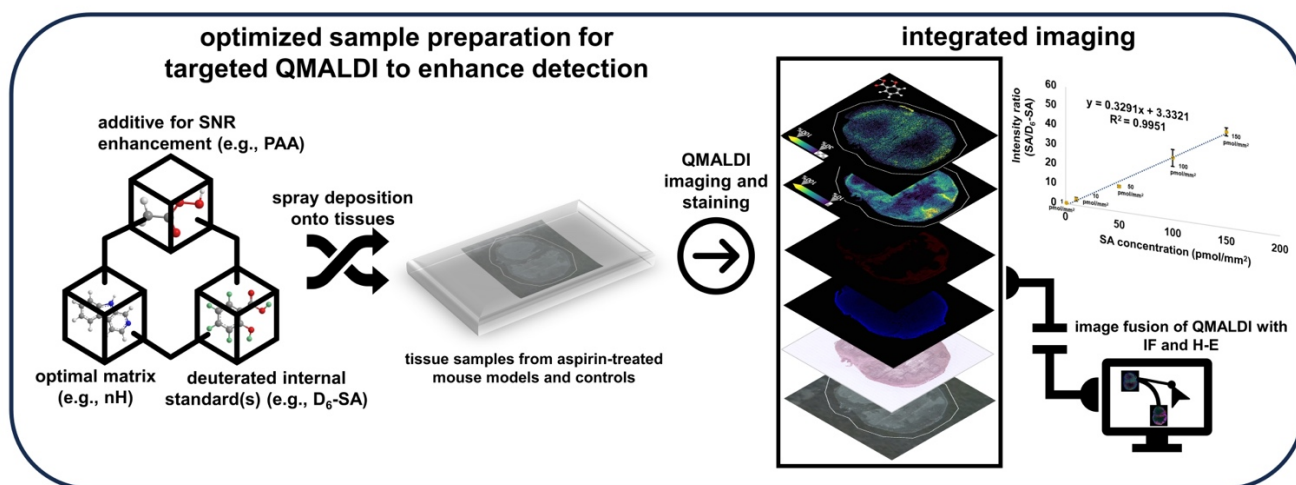


Figure 5. Schematic illustration of the integration of QMALDI imaging with hematoxylin and eosin (H-E) and CD31 immunofluorescence (IF) staining.

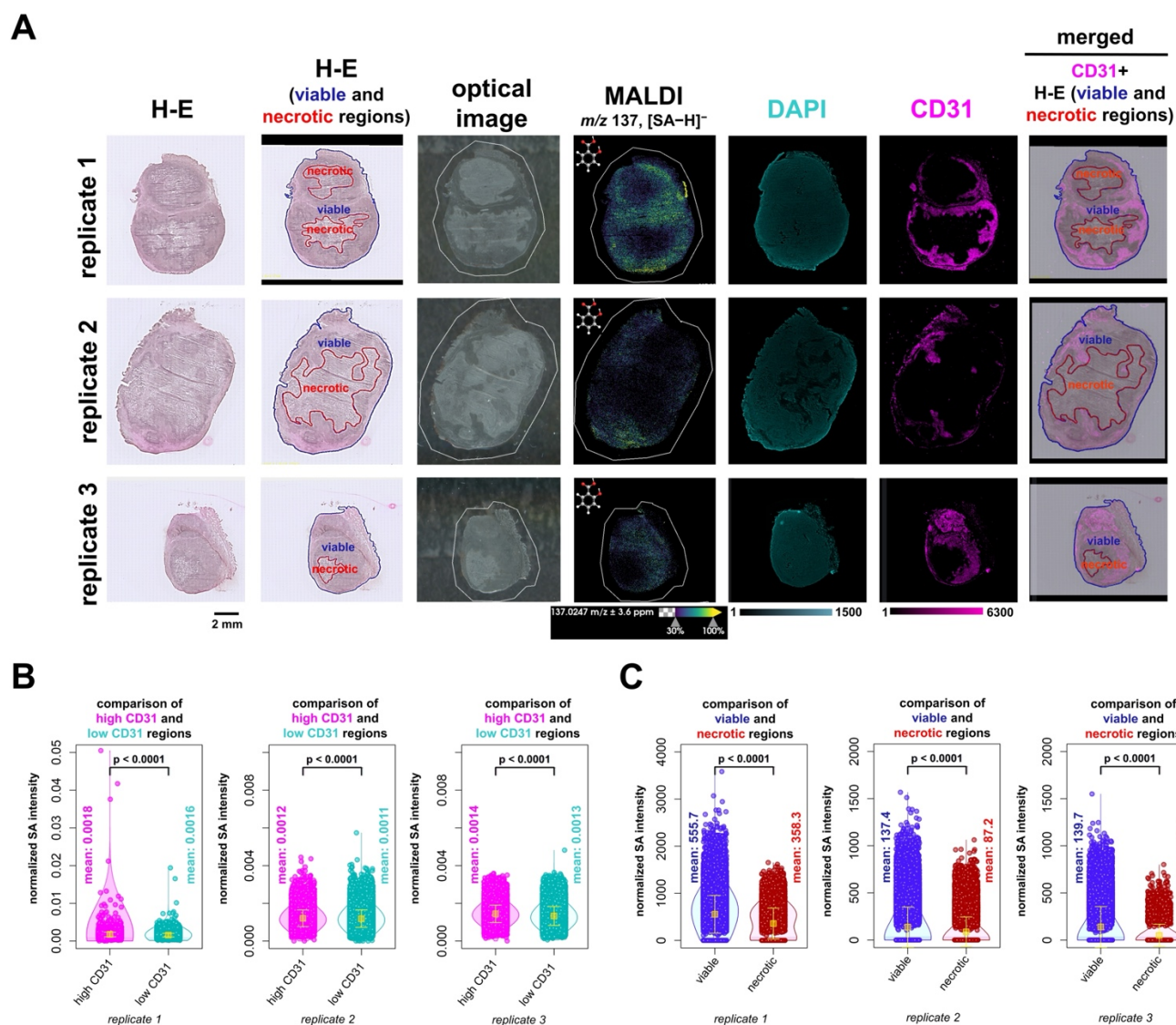
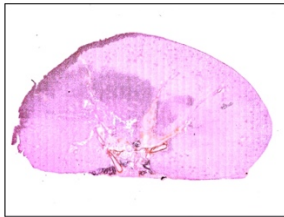
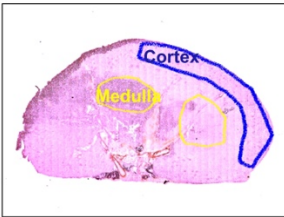
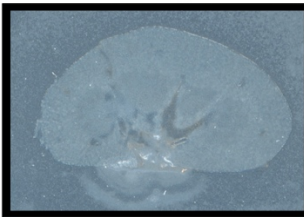
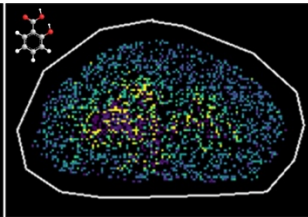
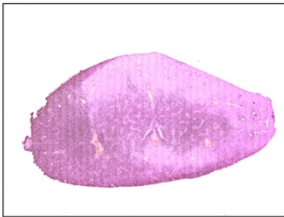
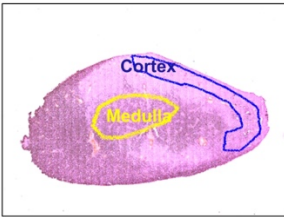
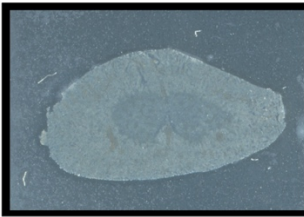
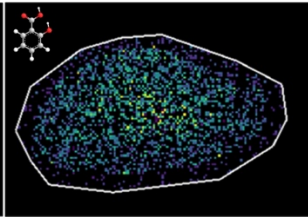
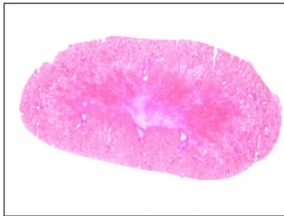
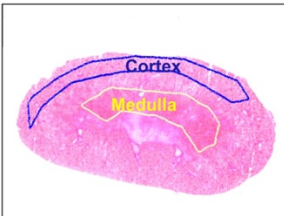
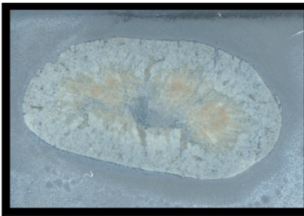
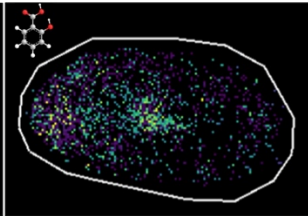


Figure 6. QMALDI SA imaging data analysis integrated with H-E and CD31 immunofluorescence staining to quantify SA content in necrotic, viable, and vascularized tumor regions. (A) The H-E and optical images are from the same tissue sections as the MALDI image, while the DAPI and CD31 images are from adjacent serial tissue sections. The figure includes three biological replicates of H-E, CD31, and DAPI-stained tumor sections, paired with MALDI images showing the spatial distribution of salicylic acid (SA) (m/z 137.02 Da, $[M-H]^-$) in tissues from aspirin-treated mice. A merged image displaying the co-registration of the CD31 image with H-E-stained viable and necrotic regions in SUM159 tumors is shown in the leftmost images. (B) DAPI and CD31 images were co-registered with and down sampled to match the MALDI imaging data, enabling precise overlay and alignment. The integration of DAPI and CD31 immunofluorescence (IF) images with MALDI images was performed using the Weave software, allowing for a detailed spatial comparison across these different imaging modalities. The integrated image was analyzed by classifying regions into high-CD31(magenta) and low-CD31 (cyan) areas, followed by

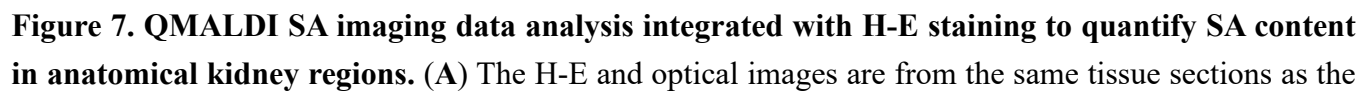
calculating the average normalized SA intensity for each region. (C) H-E-stained images of viable (blue) and necrotic (red) regions in SUM159 tumors were co-registered with MALDI images of SA using the SCiLS Lab software. The average normalized SA intensity was calculated for each region from these co-registered images. All presented measurements were performed by quantifying the SA intensity per pixel, where each open circle represents one pixel in the underlying violin plots. MALDI imaging was performed using a timsTOF fleX MALDI-2 instrument with norharmane matrix and peracetic acid additive at a 20 μm pixel size in negative ion mode. All results are also presented as mean \pm standard deviation (SD) where the mean value for each group is indicated by yellow squares.

	H-E	H-E (medulla and cortex regions)	optical image	MALDI m/z 137, [SA-H] ⁻
replicate 1				
replicate 2				
replicate 3				

2 mm

137.024 $m/z \pm 3.2$ ppm

13% 100%



MALDI image. The figure includes three biological replicates of H-E-stained kidney sections, paired with MALDI images showing the spatial distribution of salicylic acid (SA) (m/z 137.02 Da, $[M-H]^-$) in tissues from aspirin-treated mice. **(B)** H-E-stained images of medulla (yellow) and cortex (blue) regions in kidneys were co-registered with MALDI images of SA using SCiLS Lab software. The average normalized SA intensity was calculated for each region from these co-registered images. All presented measurements were performed by quantifying the SA intensity per pixel, where each open circle represents one pixel in the underlying violin plots. MALDI imaging was performed using a timsTOF fleX MALDI-2 instrument with norharmane matrix and peracetic acid additive at a 20 μ m pixel size in negative ion mode. All results are also presented as mean \pm standard deviation (SD) where the mean value for each group is indicated by yellow squares.

Abbreviation

COX: cyclooxygenase; SA: salicylic acid; CEST: chemical exchange saturation transfer; MRI: magnetic resonance imaging; DTPA: diethylenetriamine pentaacetate; DAPI: 4',6-diamidino-2-phenylindole; MALDI-MS: matrix-assisted laser desorption/ionization mass spectrometry; QMALDI: quantitative MALDI; TNBC: triple-negative breast cancer; H-E: hematoxylin and eosin; PAA: peracetic acid; nH: norharmane; SAG: salicyl acyl glucuronide; SPG: salicyl phenolic glucuronide; SU: salicyluric acid; 2,5-DHB: 2,5-dihydroxybenzoic acid; PFA: paraformaldehyde; PBS: phosphate-buffered saline; BSA: bovine serum albumin; TFA: trifluoroacetic acid; ITO: indium tin oxide; SEM: scanning electron microscopy; MSI: MALDI-MS imaging; IF: immunofluorescence; D₆-SA: D₆-salicylic acid; FL: fluorescence; SD: standard deviation.

Author Contributions

THH, MTM, and KG designed the experiments. THH, CMT, and DRB carried out sample preparation. THH and AP performed immunofluorescence staining on tissue samples. THH performed the MALDI imaging, data processing, analysis, and microscopy experiments. THH, TT and AL performed the integration of imaging modalities analysis using the WEAVE demo software. THH drafted the manuscript. THH, KG, and MTM designed the figures. THH wrote the manuscript with support from KG. All authors contributed to, provided critical feedback, reviewed, and approved the final manuscript.

Conflict of Interest

TT and AL are employees of Aspect Analytics NV. All other authors declare that they have no known competing financial interests or personal relationships that could have influenced the work reported in this paper.

Acknowledgments

The authors thank Dr. Nathan Heath Patterson, PhD and Dr. Marc Claesen, PhD (both Aspect Analytics NV) for their supervision of the data integration and analysis. We would like to acknowledge the instruments and expertise of the Johns Hopkins Applied Imaging Mass Spectrometry (AIMS) Core Facility at the Johns Hopkins University School of Medicine, which were critical in advancing this work. The authors further acknowledge funding from the National Institutes of Health (NIH) of the United States of America, grants R01 CA264901 (to KG), P30 CA006973 Shared Resource for Mass Spectrometry

Molecular Imaging and Multi-Omics (to KG), S10 OD030500 (to KG), R01 CA196701 (to APP), R01 CA237597 (to APP), P41 EB024495 (to MTM), R01 CA285792 (to MTM).

Code Availability.

All data analysis codes used in this study are available on GitHub: https://github.com/TaehunHahm/SA-paper_NewVioplot_TH.git

References

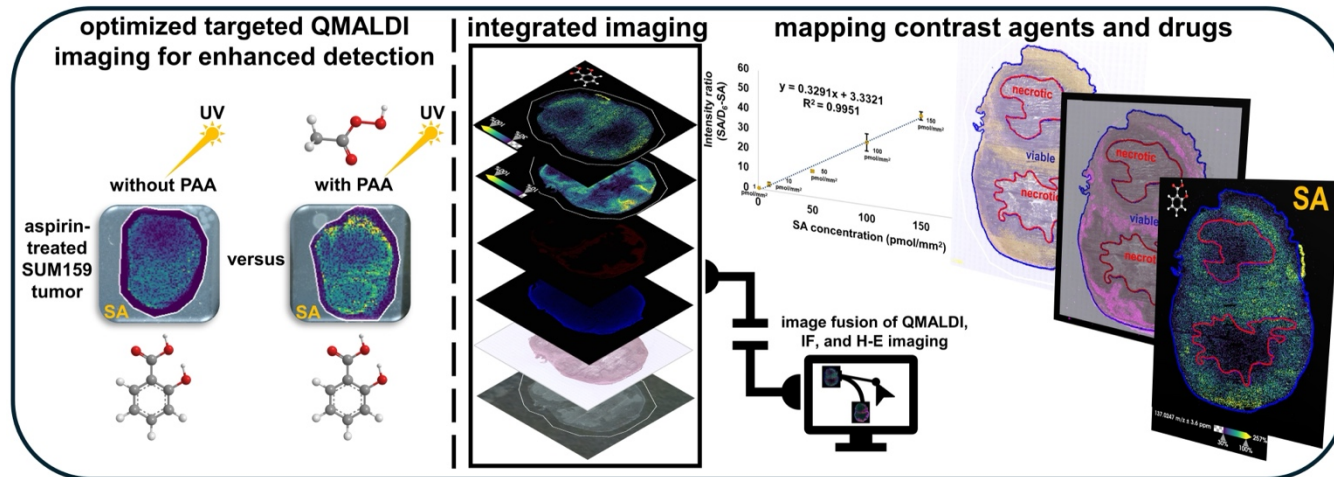
- [1] Vane JR. Inhibition of prostaglandin synthesis as a mechanism of action for aspirin-like drugs. *Nat. Cell Biol.* 1971; 231: 232–5.
- [2] Fitzgerald DJ, FitzGerald GA. Historical lessons in translational medicine. *Circ. Res.* 2013; 112: 174–94.
- [3] Amann R, Peskar BA. Anti-inflammatory effects of aspirin and sodium salicylate. *Eur. J. Pharmacol.* 2002; 447: 1–9.
- [4] Bannwarth B, Demotes-Mainard F, Schaefferbeke T, Labat L, Dehais J. Central analgesic effects of aspirin-like drugs. *Fundam. Clin. Pharmacol.* 1995; 9: 1–7.
- [5] Mahdi JG, Mahdi AJ, Mahdi AJ, Bowen ID. The historical analysis of aspirin discovery, Its relation to the willow tree and antiproliferative and anticancer potential. *Cell Prolif.* 2006; 39: 147–55.
- [6] Desborough MJR, Keeling DM. The aspirin story – from willow to wonder drug. *Br. J. Haematol.* 2017; 177: 674–83.
- [7] Banerjee SR, Song X, Yang X, Minn I, Lisok A, Chen Y, et al. Salicylic acid-based polymeric contrast agents for molecular magnetic resonance imaging of prostate cancer. *Chem. Eur. J.* 2018; 24: 7235–42.
- [8] Lesniak WG, Oskolkov N, Song X, Lal B, Yang X, Pomper MG, et al. Salicylic acid conjugated dendrimers are a tunable, high performance CEST MRI nanoplatfrom. *Nano Lett.* 2016; 16: 2248–53.
- [9] Pavuluri KD, Yang E, Ayyappan V, Sonkar K, Tan Z, Tressler CM, et al. Unlabeled aspirin as an activatable theranostic MRI agent for breast cancer. *Theranostics* 2022; 12: 1937–51.
- [10] Yang X, Song X, Li Y, Liu G, Banerjee SR, Pomper MG, et al. Salicylic acid and analogues as diaCEST MRI contrast agents with highly shifted exchangeable proton frequencies. *Angew. Chem.* 2013; 125: 8274–7.
- [11] Yang X, Yadav NN, Song X, Banerjee SR, Edelman H, Minn I, et al. Tuning phenols with intra-molecular bond shifted hydrogens (IM-SHY) as diaCEST MRI contrast agents. *Chem. Eur. J.* 2014; 20: 15824–32.
- [12] Li J, Feng X, Zhu W, Oskolkov N, Zhou T, Kim BK, et al. Chemical exchange saturation transfer (CEST) agents: quantum chemistry and MRI. *Chem. Eur. J.* 2015; 22: 264–71.

- [13] Brune K, Rainsford KD, Schweitzer A. Biodistribution of mild analgesics. *Br. J. Clin. Pharmacol.* 1980; 10: 279S–84S.
- [14] Stevens H, Voelker M, Gow L, MacDougall F, Bieri G. In-vivo disintegration and absorption of two fast acting aspirin tablet formulations compared to ibuprofen tablets using pharmacoscintigraphy. *J. Drug Deliv. Sci. Technol.* 2019; 51: 535–41.
- [15] Wilding IR, Hardy JG, Sparrow RA, Davis SS, Daly PB, English JR. In vivo evaluation of enteric-coated naproxen tablets using gamma scintigraphy. *Pharm. Res.* 1992; 9: 1436–41.
- [16] Visagie JL, Aruwajoye GS, van der Sluis R. Pharmacokinetics of aspirin: evaluating shortcomings in the literature. *Expert Opin. Drug Metab. Toxicol.* 2024; 20: 727–40.
- [17] Chen Z, Han Z, Liu G. Repurposing clinical agents for chemical exchange saturation transfer magnetic resonance imaging: current status and future perspectives. *Pharmaceuticals* 2020; 14: 11.
- [18] Mascini NE, Cheng M, Jiang L, Rizwan A, Podmore H, Bhandari DR, et al. Mass spectrometry imaging of the hypoxia marker pimonidazole in a breast tumor model. *Anal. Chem.* 2016; 88: 3107–14.
- [19] Zivko C, Hahm T, Tressler C, Brown D, Glunde K, Mahairaki V, et al. Mass spectrometry imaging of organoids to improve preclinical research. *Adv. Healthc. Mater.* 2024; 13: 2302499.
- [20] Hahm TH, Matsui T, Tanaka M. Matrix-assisted laser desorption/ionization mass spectrometry imaging of tissues via the formation of reproducible matrix crystals by the fluorescence-assisted spraying method: a quantification approach. *Anal. Chem.* 2022; 94: 1990–8.
- [21] Bungert D, Heinzle E, Tholey A. Quantitative matrix-assisted laser desorption/ionization mass spectrometry for the determination of enzyme activities. *Anal. Biochem.* 2004; 326: 167–75.
- [22] Abu Sammour D, Marsching C, Geisel A, Erich K, Schulz S, Guevara CR, et al. Quantitative mass spectrometry imaging reveals mutation status-independent lack of imatinib in liver metastases of gastrointestinal stromal tumors. *Sci. Rep.* 2019; 9: 10698.
- [23] Vandenbosch M, Mutuku SM, Mantas MJQ, Patterson NH, Hallmark T, Claesen M, et al. Toward omics-scale quantitative mass spectrometry imaging of lipids in brain tissue using a multiclass internal standard mixture. *Anal. Chem.* 2023; 95:18719–30.

- [24] Krutchinsky AN, Chait BT. On the nature of the chemical noise in MALDI mass spectra. *J. Am. Soc. Mass Spectrom.* 2002; 13: 129–34.
- [25] Caretti C, Lubello C. Wastewater disinfection with PAA and UV combined treatment: a pilot plant study. *Water Res.* 2003; 37: 2365–73.
- [26] Kiejza D, Kotowska U, Polińska W, Karpińska J. Peracids - new oxidants in advanced oxidation processes: the use of peracetic acid, peroxymonosulfate, and persulfate salts in the removal of organic micropollutants of emerging concern – a review. *Sci. Total Environ.* 2021; 790: 148195.
- [27] Cai M, Sun P, Zhang L, Huang C. UV/peracetic acid for degradation of pharmaceuticals and reactive species evaluation. *Environ. Sci. Technol.* 2017; 51: 14217–24.
- [28] Zaleski J, Daszkiewicz Z, Kyziół JB. Structure of N,4-dinitroaniline and its complex with sulfolane at 85 K; on the proton donor–acceptor affinity of the primary nitramine (HNNO₂) group. *Acta Cryst.* 2001; B58: 109–15.
- [29] Quinn JR, Zimmerman SC, Del Bene JE, Shavitt I. Does the A·T or G·C base-pair possess enhanced stability? quantifying the effects of CH···O interactions and secondary interactions on base-pair stability using a phenomenological analysis and ab initio calculations. *J. Am. Chem. Soc.* 2007; 129: 934–41.
- [30] Lemaire R, Tabet JC, Ducoroy P, Hendra JB, Salzert M, Fournier I. Solid ionic matrices for direct tissue analysis and MALDI imaging. *Anal. Chem.* 2006; 78: 809–19.
- [31] Tressler C, Tilley S, Yang E, Donohue C, Barton E, Creissen A, et al. Factorial design to optimize matrix spraying parameters for MALDI mass spectrometry imaging. *J. Am. Soc. Mass Spectrom.* 2021; 32: 2728–37.
- [32] Shen B, Jensen RG, Bohnert HJ. Mannitol protects against oxidation by hydroxyl radicals. *Plant Physiol.* 1997; 115: 527–32.
- [33] Pirman DA, Reich RF, Kiss A, Heeren RM, Yost RA. Quantitative MALDI tandem mass spectrometric imaging of cocaine from brain tissue with a deuterated internal standard. *Anal. Chem.* 2013; 85: 1081–9.

- [34] Hamm G, Bonnel D, Legouffe R, Pamelard F, Delbos J, Bouzom F, et al. Quantitative mass spectrometry imaging of propranolol and olanzapine using tissue extinction calculation as normalization factor. *J. Proteomics*. 2012; 75: 4952–61.
- [35] Bąchor R, Kluczyk A, Stefanowicz P, Szewczuk Z. Preparation of novel deuterated cyclosporin A standards for quantitative LC-MS analysis. *J. Mass Spectrom*. 2017; 52: 817–22.
- [36] Martin IB, Henry LC, Joseph JK. Studies with deuterated drugs. *Pharm. Sci*. 1975; 64: 367–91.
- [37] Hatori A, Shigematsu A, Tsuya A. The metabolism of aspirin in rats; localization, absorption, distribution, and excretion. *Eur. J. Drug Metab. Pharmacokinet*. 1984; 9: 205–14.
- [38] Levy G. Clinical pharmacokinetics of aspirin. *Pediatrics*. 1978; 62: 867–72.
- [39] Chumbley CW, Reyzer ML, Allen JL, Marriner GA, Via LE, Barry CE III, et al. Absolute quantitative MALDI imaging mass spectrometry: A case of rifampicin in liver tissues. *Anal. Chem*. 2016; 88: 2392–8.

Table of content



Supporting Information

Quantitative MALDI imaging of aspirin metabolites in mouse models of triple-negative breast cancer

Tae-Hun Hahm,^{a,b} Dalton R. Brown,^a Caitlin M. Tressler,^{a,b} Thao Tran,^c Alice Ly,^c Arvind P. Pathak^b, Michael T. McMahon,^{b,c} Kristine Glunde,^{*, a,b,d,f}

^a The Johns Hopkins Applied Imaging Mass Spectrometry Core and Service Center, Division of Cancer Imaging Research,

^b The Russell H. Morgan Department of Radiology and Radiological Science, The Johns Hopkins University School of Medicine, Baltimore, MD 21205, USA

^c Aspect Analytics NV, C-mine 12, 3600 Genk, Belgium

^d The Sidney Kimmel Comprehensive Cancer Center, The Johns Hopkins University School of Medicine, Baltimore, MD 21205, USA Aspect

^e F.M. Kirby Research Center for Functional Brain Imaging, Kennedy Krieger Institute, Baltimore, MD 21205, USA

^f Department of Biological Chemistry, The Johns Hopkins University School of Medicine, Baltimore, MD 21205, USA

Table of Contents

Supplementary Figures

Figure S1. Effect of PAA concentration on SA fragment ion (m/z 93.03 Da) detection in tissue samples.....	S3
Figure S2. Comparison of experimental conditions: Matrix and SA signals in liver tissues with or without PAA	S4
Figure S3. Comparison of experimental conditions: Matrix and SA signals in kidney tissues with or without PAA	S5
Figure S4. Comparison of experimental conditions: Matrix and SA signals in SUM159 tumor tissues with or without PAA	S6
Figure S5. MS/MS spectrum of m/z 154.97 in negative ion mode, generated from the norharmane matrix	S7
Figure S6. MS/MS spectrum of m/z 248.96 in negative ion mode, generated from the norharmane matrix	S8
Figure S7. Hydroxyl radical scavenging experiment to validate PAA mechanism in MALDI imaging	S9-S10
Figure S8. MALDI imaging of aspirin distribution in tissue sections from aspirin treated versus untreated control mice...	S11
Figure S9. MALDI imaging of 2,5-DHB distribution in tissue sections from aspirin treated versus untreated control mice	S12
Figure S10. MALDI imaging of SAG distribution in tissue sections from aspirin treated versus untreated control mice	S13
Figure S11. MALDI imaging of SPG distribution in tissue sections from aspirin treated versus untreated control mice....	S14
Figure S12. MALDI imaging of SU distribution in tissue sections from aspirin treated versus untreated control mice.....	S15
Figure S13. MS/MS spectra in negative ion mode for m/z 137.02, identified as SA	S16
Figure S14. MS/MS spectra in negative ion mode for m/z 179.03, identified as aspirin	S17
Figure S15. MS/MS spectra in negative ion mode for m/z 153.02, identified as 2,5-DHB	S18
Figure S16. Comprehensive workflow map for SA quantification in tissue samples by MALDI-MSI	S19
Figure S17. MALDI imaging analysis of sprayed on D ₆ -SA and tissue-contained SA in liver, kidney, and SUM159 tumor tissue sections.....	S20
Figure S18. Microscopic images of liver sections stained with Hematoxylin-Eosin (H-E), alongside MALDI imaging.....	S21

Supplementary Figures

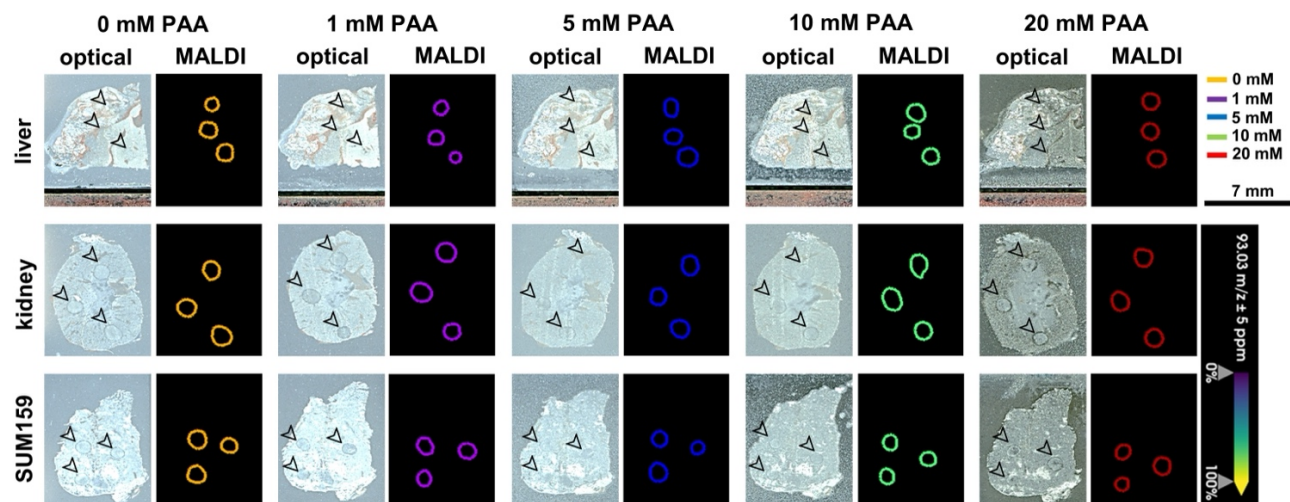


Figure S1. Effect of PAA concentration on SA fragment ion (m/z 93.03 Da) detection in tissue samples. Optical and MALDI images of tissue sections spotted with dried droplets of 1 mM salicylic acid (SA) followed by application of norharmane (nH), combined with varying concentrations of peracetic acid (PAA) (0 mM, 1 mM, 5 mM, 10 mM, and 20 mM). Black arrows indicate the locations of the dried SA droplets in the optical images. Matrix-Assisted Laser Desorption/Ionization (MALDI) images were acquired at 100 μ m pixel size in negative ion mode using a timsTOF fleX MALDI-2 instrument. The data demonstrate that the SA fragment ion at $[M-H]^- = m/z$ 93.03 Da was not detected in the dried droplets spotted on tissue sections.

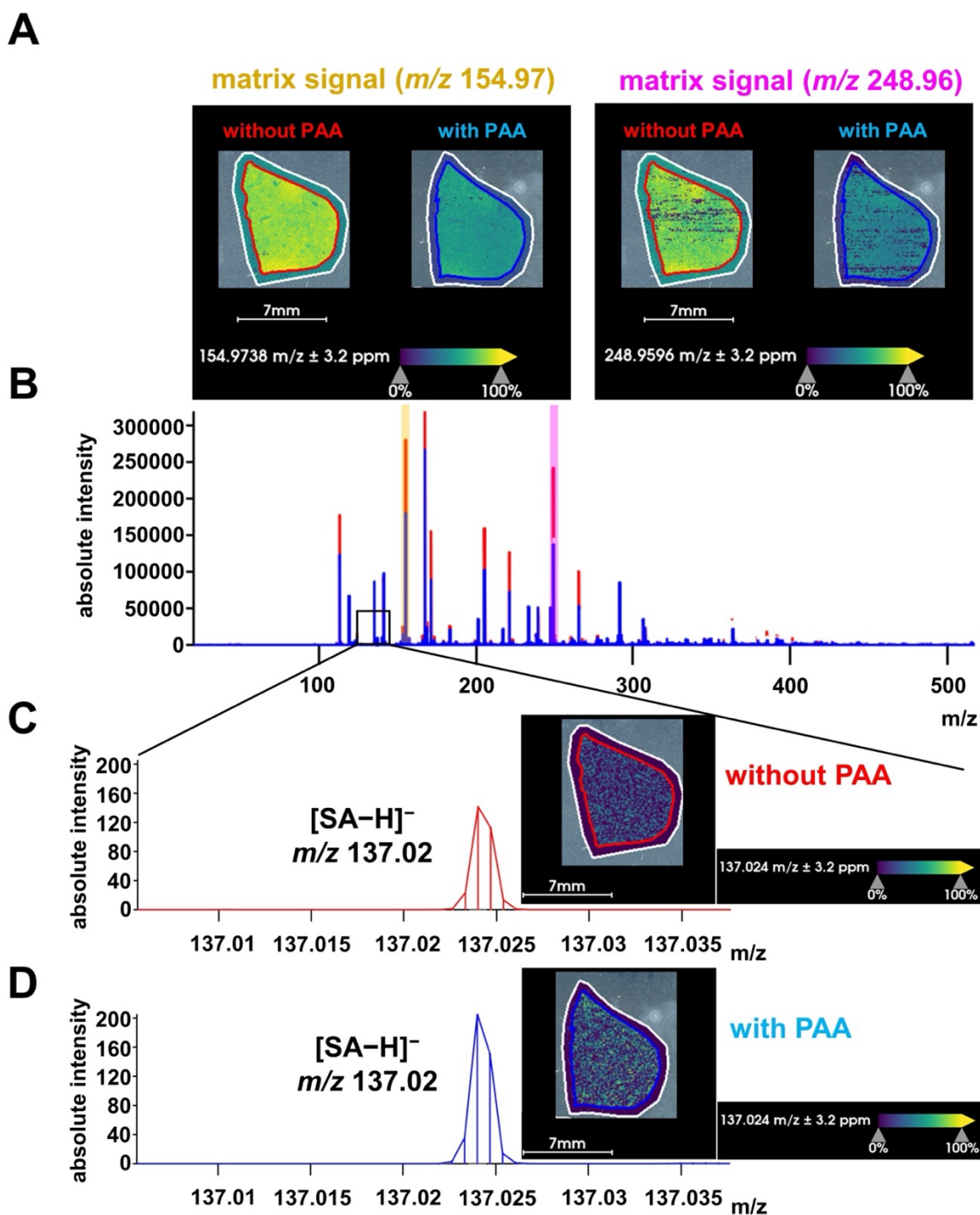


Figure S2. Comparison of experimental conditions: Matrix and SA signals in liver tissues with or without PAA. (A) MALDI images showing the two highest matrix background signals at m/z 154.97 Da and m/z 248.96 Da, and (B) corresponding average spectra ranging from m/z 0–500 Da in liver sections from aspirin-treated mouse mice following norharmane application, either with (blue spectra) or without (red spectra) 5 mM PAA. The MALDI images were acquired at 100 μ m pixel size in negative ion mode using a timsTOF fleX MALDI-2 instrument. The data demonstrate that the [M-H]⁻ ion of SA at m/z 137.02 Da was detected in tissue sections from aspirin treated mice after norharmane application (C) with or (D) without 5 mM PAA, which resulted in a higher SA signal intensity when PPA was applied.

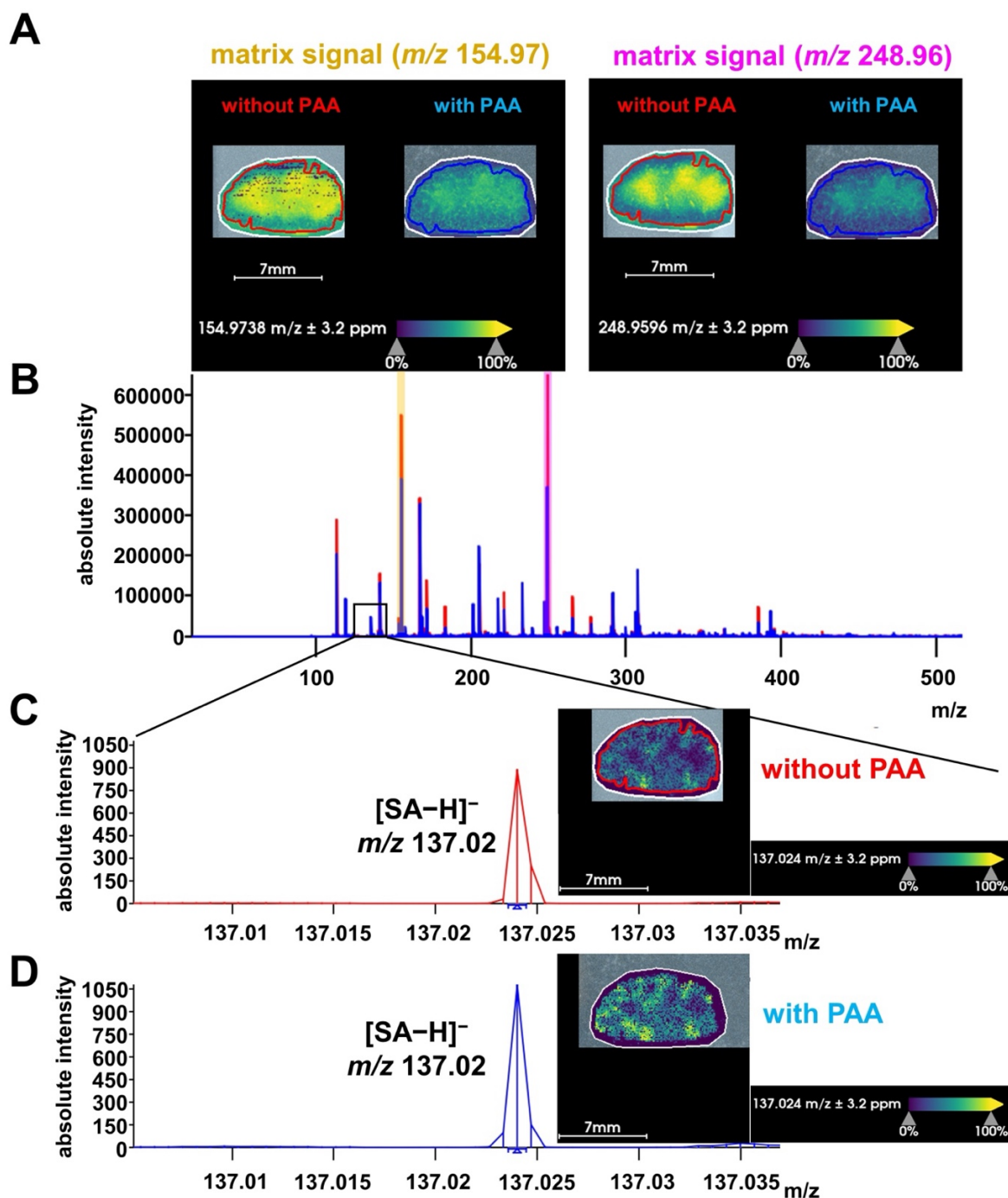


Figure S3. Comparison of experimental conditions: Matrix and SA signals in kidney tissues with or without PAA. (A) MALDI images showing the two highest matrix background signals at m/z 154.97 Da and m/z 248.96 Da, and (B) corresponding average spectra ranging from m/z 0–500 Da in kidney sections from aspirin-treated mice following norharmane application, either with (blue spectra) or without (red spectra) 5 mM PAA. The MALDI images were acquired at 100 μ m pixel size in negative ion mode using a timsTOF fleX MALDI instrument. The data demonstrate that the [M-H]⁻ ion of SA at m/z 137.02 Da was detected in tissue sections from aspirin treated mice after norharmane application (C) with or (D) without 5 mM PAA, which resulted in a higher SA signal intensity when PAA was applied.

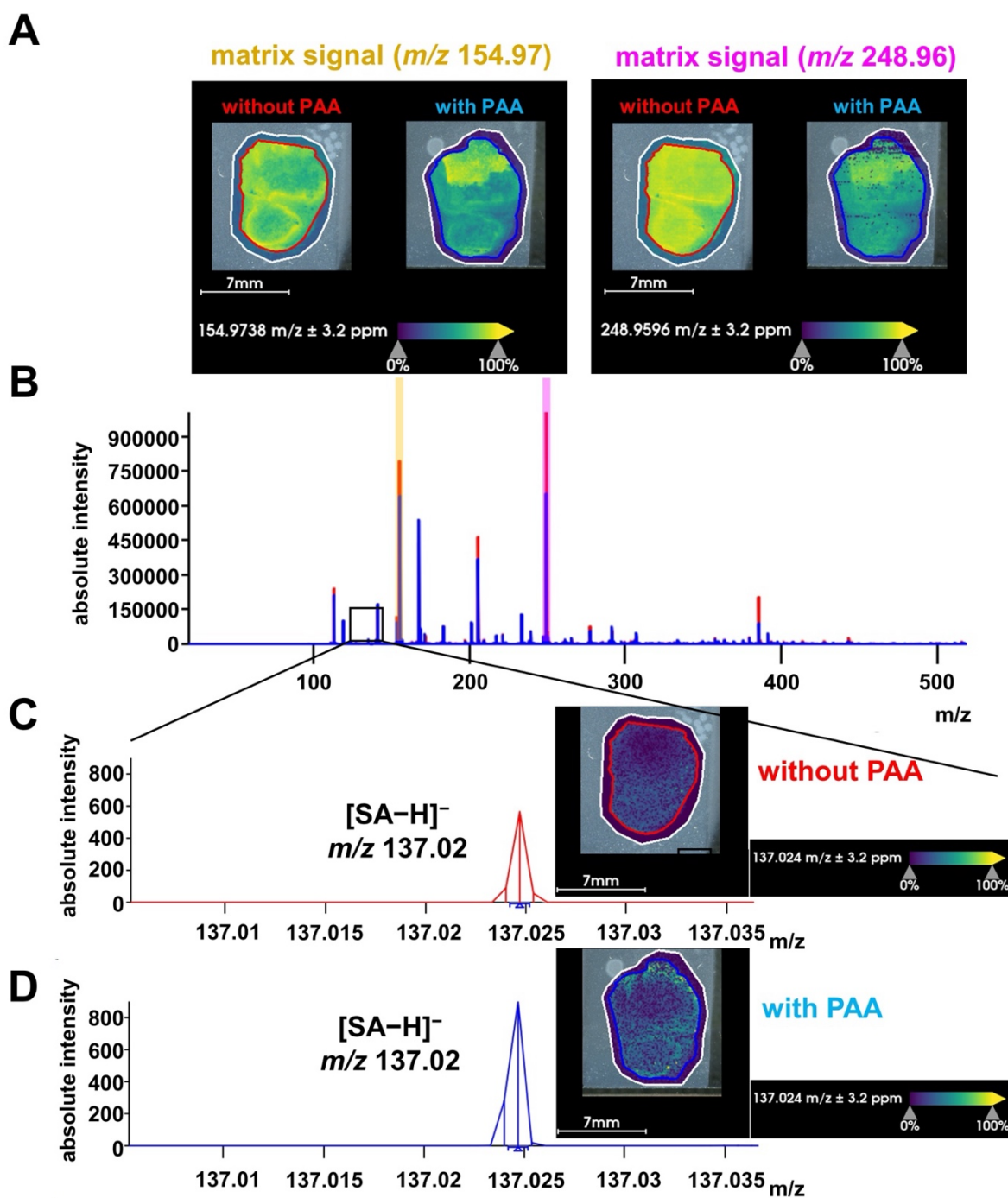


Figure S4. Comparison of experimental conditions: Matrix and SA signals in SUM159 tumor tissues with or without PAA. (A) MALDI images showing the two highest matrix background signals at m/z 154.97 Da and m/z 248.96 Da, and (B) corresponding average spectra ranging from m/z 0–500 Da in SUM159 tumor sections from aspirin-treated mice tissue following norharmane application, either with (blue spectra) or without (red spectra) 5 mM PAA. The MALDI images were acquired with a 100 μ m pixel size in negative ion mode using a timsTOF fleX MALDI-2 instrument. The data demonstrate that the [M-H]⁻ ion of SA at m/z 137.02 Da was detected in tissue sections from aspirin treated mice after norharmane application (C) with or (D) without 5 mM PAA, which resulted in a higher SA signal intensity when PPA was applied.

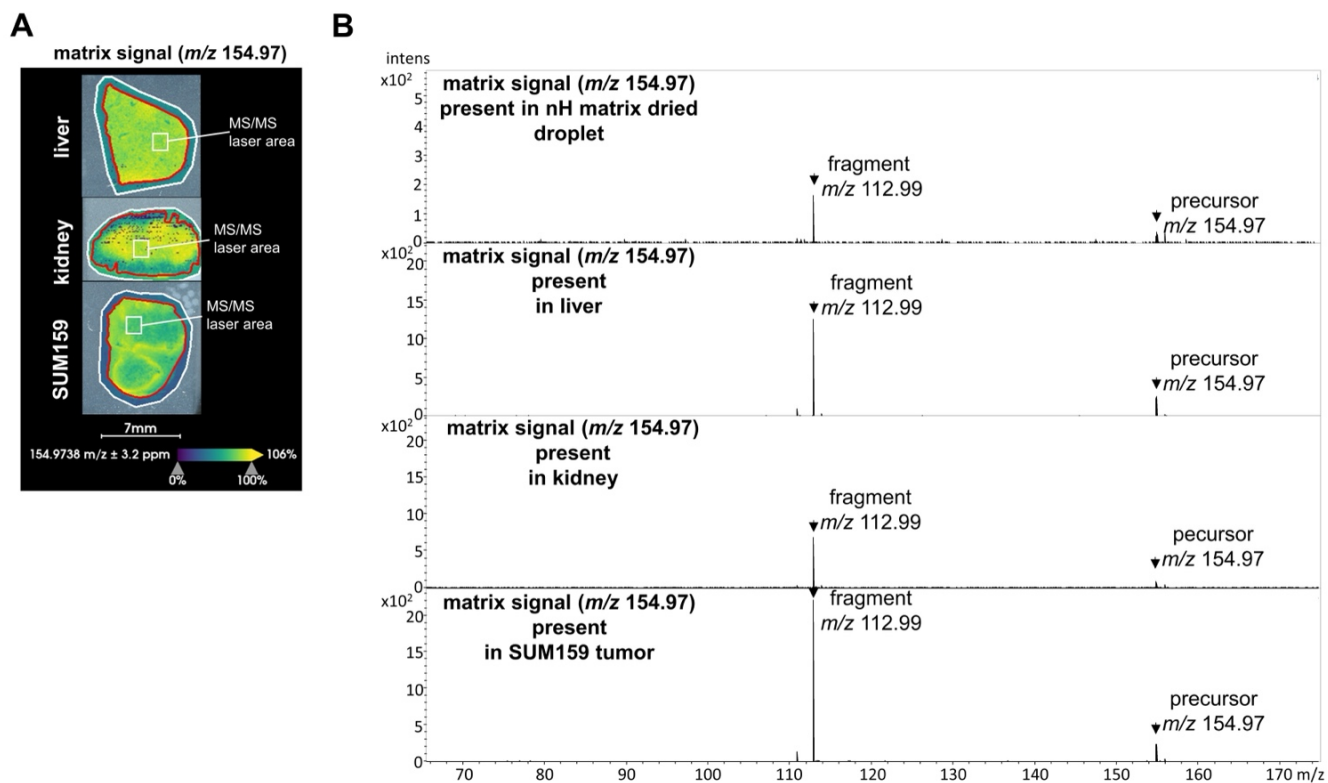


Figure S5. MS/MS spectrum of m/z 154.97 in negative ion mode, generated from the norharmane matrix. (A) The MS/MS laser area used for the analysis is highlighted with a white box. The (A) spatial distribution and (B) precursor peak at m/z 154.97 Da, and its fragment ion at m/z 112.99 Da are shown for a dried norharmane (nH) droplet, as well as for liver, kidney, and SUM159 tumor sections.

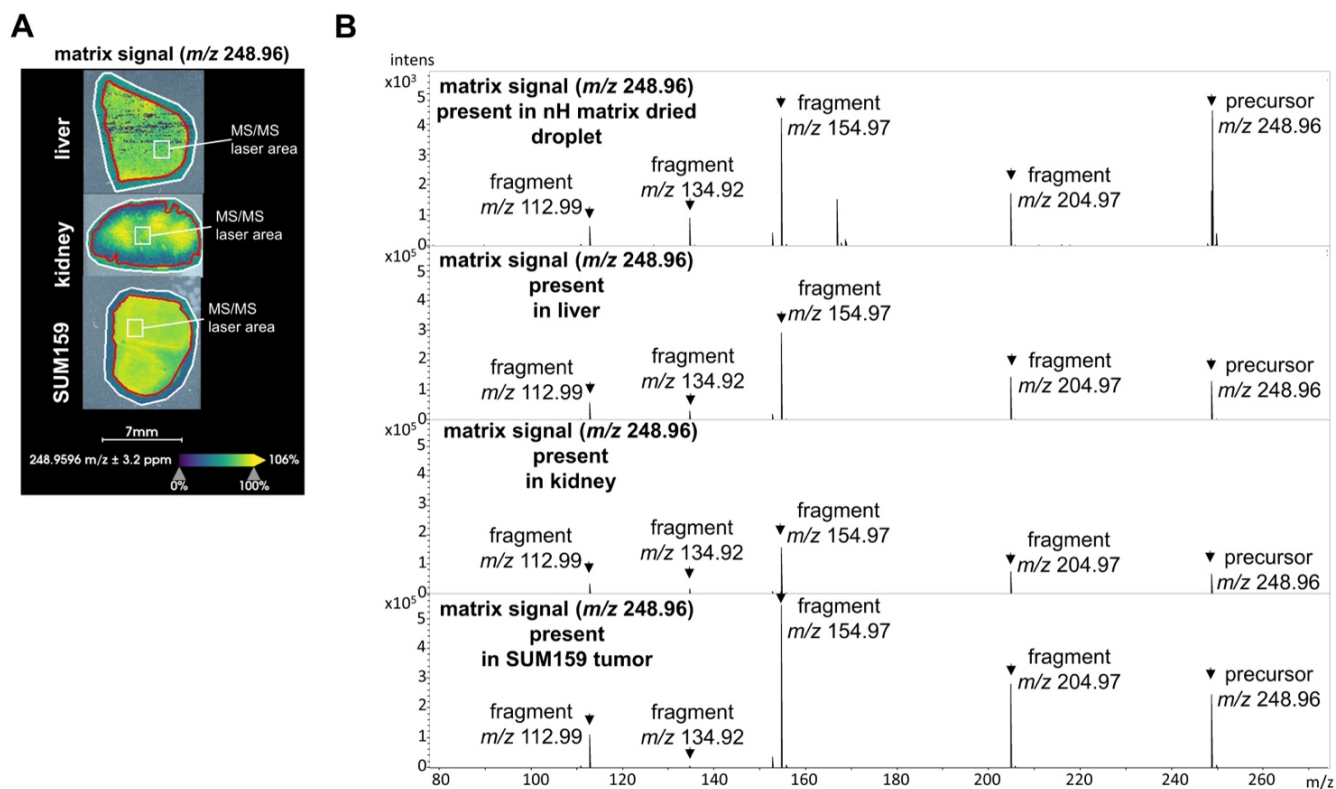


Figure S6. MS/MS spectrum of m/z 248.96 in negative ion mode, generated from the norharmane matrix. (A) The MS/MS laser area used for the analysis is highlighted with a white box. The (A) spatial distribution and (B) precursor peak at m/z 248.96 Da, and its fragment ions at m/z 112.99, 134.92, 154.97, and 204.97 Da are shown for a dried norharmane (nH) droplet, as well as for liver, kidney, and SUM159 tumor sections.

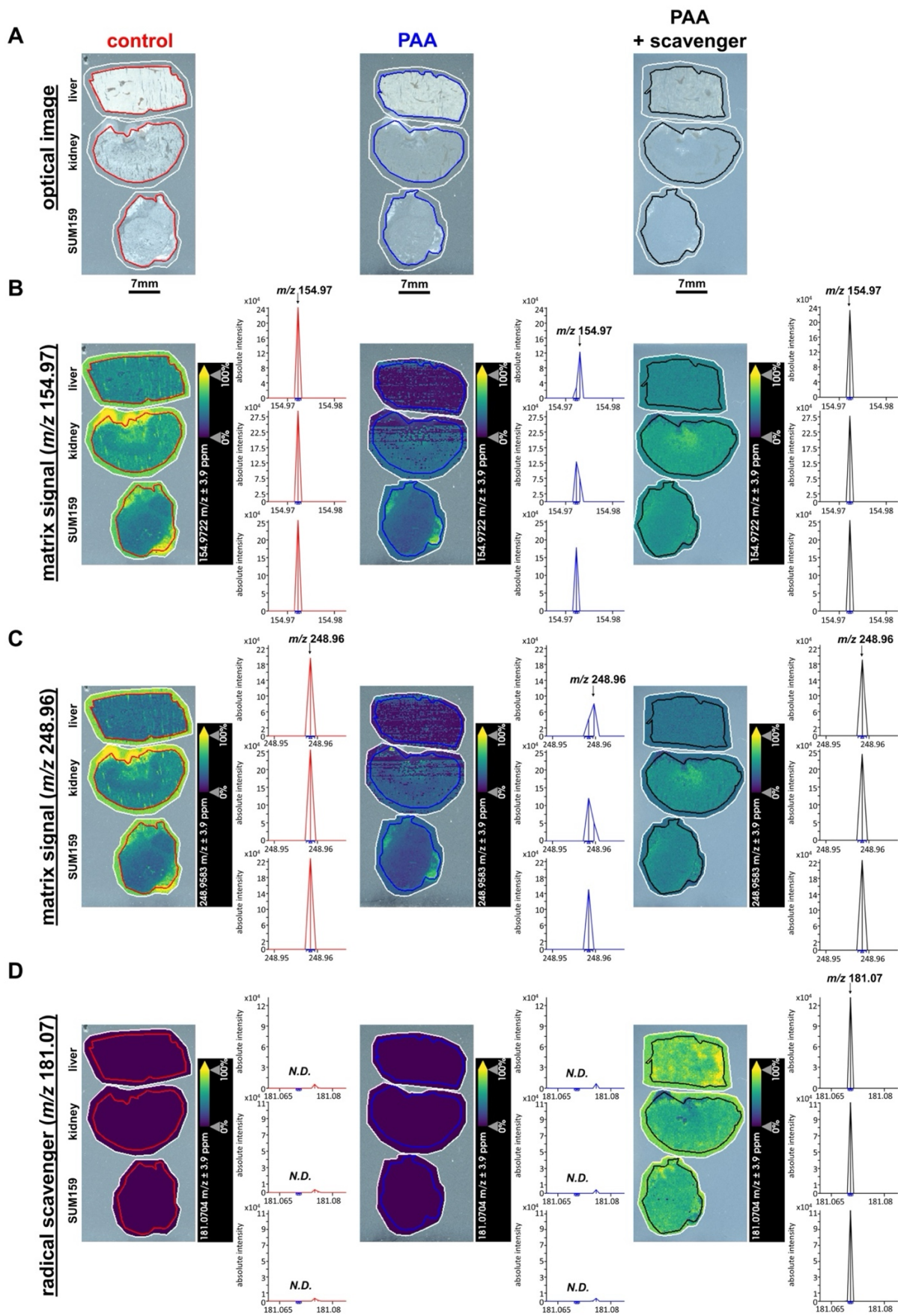


Figure S7. Hydroxyl radical scavenging experiment to validate PAA mechanism in MALDI imaging. (A) Optical images of tissue sections after matrix application showing crystal morphology under three experimental conditions: Control (nH matrix only), PAA (nH matrix + 5 mM PAA), and PAA + scavenger (nH matrix + 5 mM PAA + 100 mM D-mannitol). Images demonstrate uniform matrix deposition across all conditions in liver, kidney, and SUM159 tumor tissues. (B) MALDI imaging and corresponding mass spectra of matrix background signal at m/z 154.97 across the three experimental conditions. Left panels show spatial maps of the two indicated matrix and scavenger m/z values, while right panels display representative spectra from liver, kidney, and SUM159 tumor tissues. Adding PAA to the matrix results in reduced matrix signal intensity compared to matrix-only control, while with the addition of the radical scavenger D-mannitol and PAA to the matrix, matrix signals are restored, indicating hydroxyl radical involvement in matrix ion suppression. (C) MALDI imaging and corresponding mass spectra of matrix background signal at m/z 248.96 across the three experimental conditions. Similar to panel B, the data show PAA-induced signal reduction and D-mannitol-mediated signal recovery, providing additional evidence for hydroxyl radical-mediated matrix background suppression. (D) MALDI imaging and corresponding mass spectra of D-mannitol ($[M-H]^-$, m/z 181.07) confirms that the presence of D-mannitol for PAA + scavenger. Ion intensity maps and spectra from MALDI imaging data of liver, kidney, and SUM159 tumor tissues confirm the successful incorporation and detection of the hydroxyl radical scavenger D-mannitol in tissue sections to which it was applied in the experimental group of PAA + scavenger. *N.D.: Not detected.

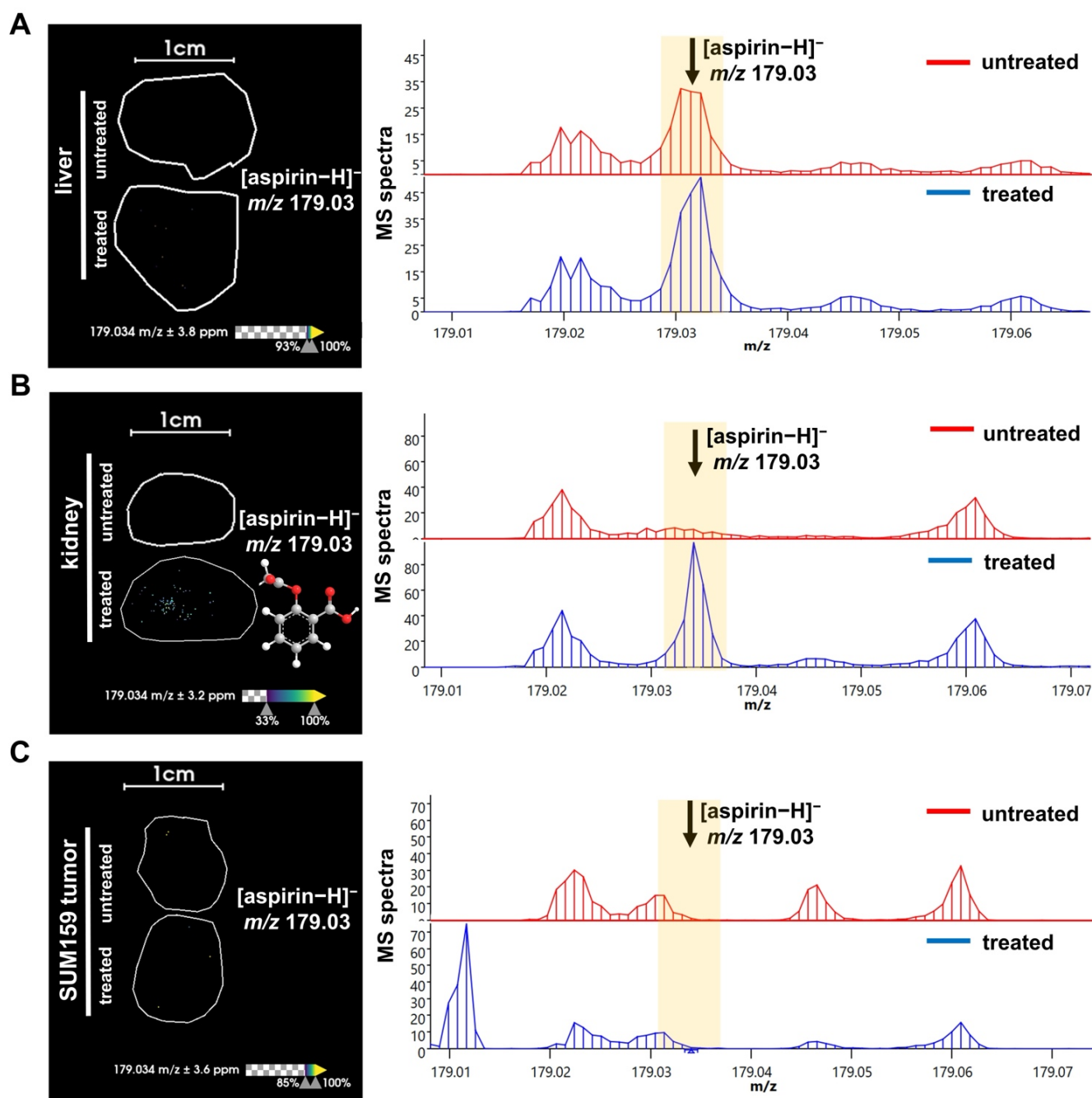


Figure S8. MALDI imaging of aspirin distribution in tissue sections from aspirin treated versus untreated control mice. MALDI imaging and corresponding average spectra of aspirin distribution in representative (A) liver, (B) kidney, and (C) SUM159 tumor sections from 300 mM aspirin-treated (bottom, blue spectra) and untreated control (top, red spectra) mice. The data clearly show that the [M-H]⁻ ion of aspirin at m/z 179.03 Da was detected in kidney tissue sections, but not in tumor and liver sections from aspirin treated mice, while tissues from untreated mice showed no aspirin signal or comparable noise signal at this m/z value, indicating that the detected signal represents noise signal rather than specific aspirin detection. The MALDI images were acquired at 100 μ m pixel size in negative ion mode using a timsTOF fleX MALDI-2 instrument with norharmane matrix and PAA as an additive.

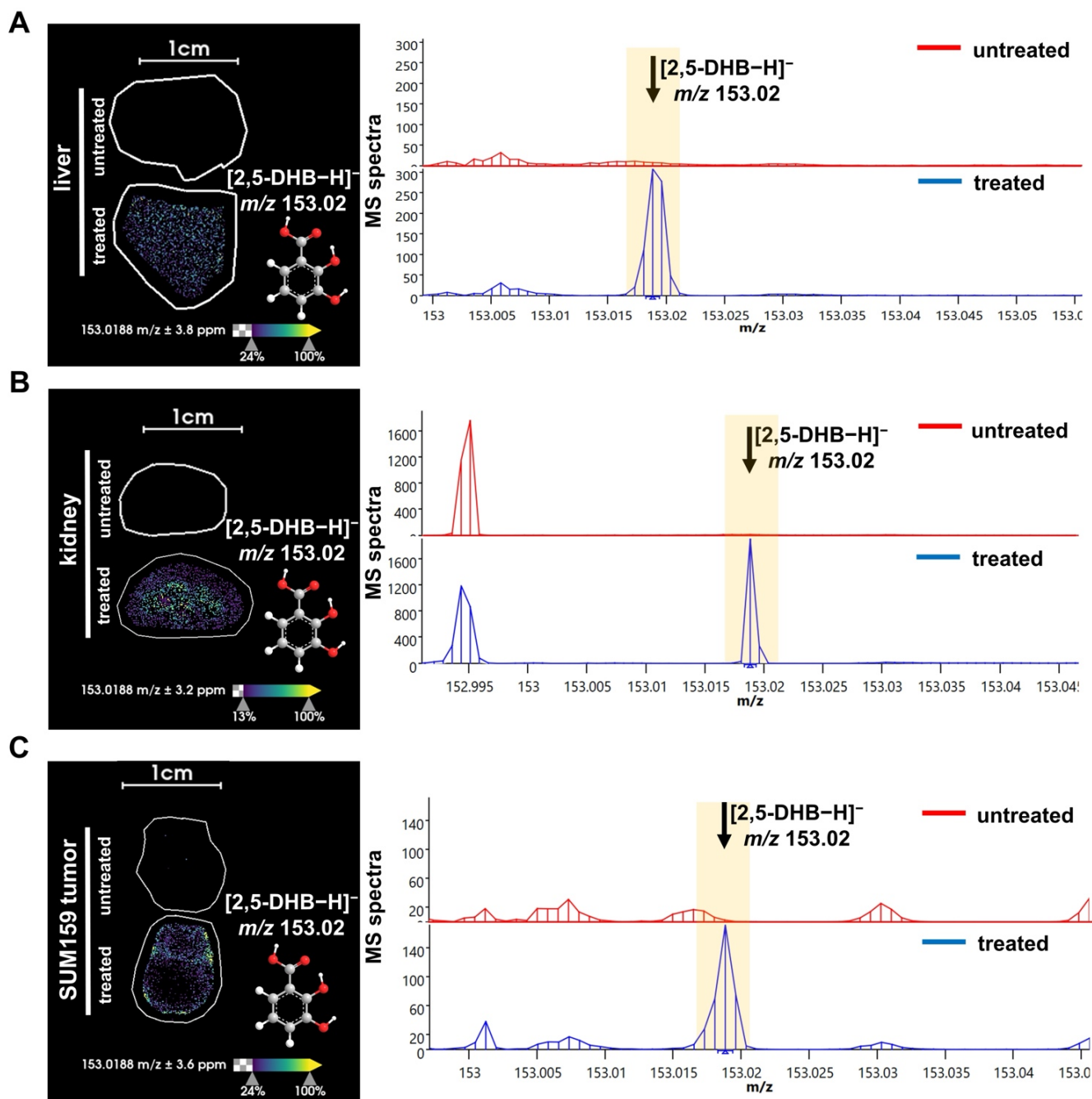


Figure S9. MALDI imaging of 2,5-DHB distribution in tissue sections from aspirin treated versus untreated control mice. MALDI imaging and corresponding average spectra of 2,5-DHB distribution in representative (A) liver, (B) kidney, and (C) SUM159 tumor sections from 300 mM aspirin-treated (bottom, blue spectra) and untreated control (top, red spectra) mice. The data clearly show that the [M-H]⁻ ion of 2,5-DHB at m/z 153.02 Da was detected in SUM159 tumor, kidney, and liver tissue sections from aspirin treated mice, while it was absent in all tissues from untreated control mice. The MALDI images were acquired at 100 μ m pixel size in negative ion mode using a timsTOF fleX MALDI-2 instrument with norharmane matrix and PAA as an additive.

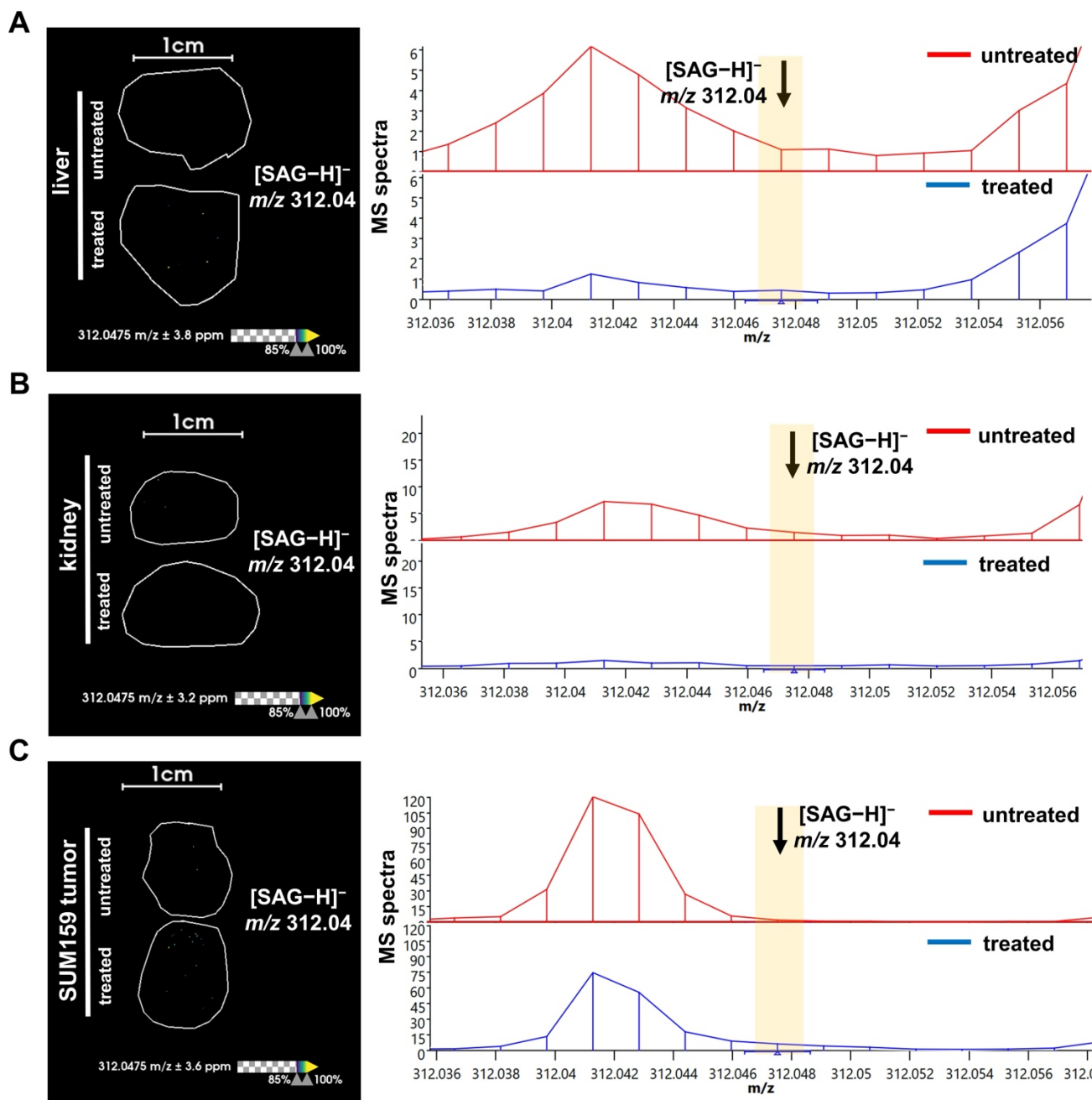


Figure S10. MALDI imaging of salicyl acyl- β -D-glucuronide (SAG) distribution in tissue sections from aspirin treated versus untreated control mice. MALDI imaging and corresponding average spectra of SAG distribution in (A) liver, (B) kidney, and (C) SUM159 tumor sections from 300 mM aspirin-treated (bottom, blue spectra) and untreated control (top, red spectra) mice. The data show that the $[M-H]^-$ ion of SAG at m/z 312.04 Da was not detected in any tissues, neither in tissues from aspirin treated mice nor in those from untreated control mice. The MALDI images were acquired at 100 μ m pixel size in negative ion mode using a timsTOF fleX MALDI-2 instrument with norharmane matrix and PAA as an additive.

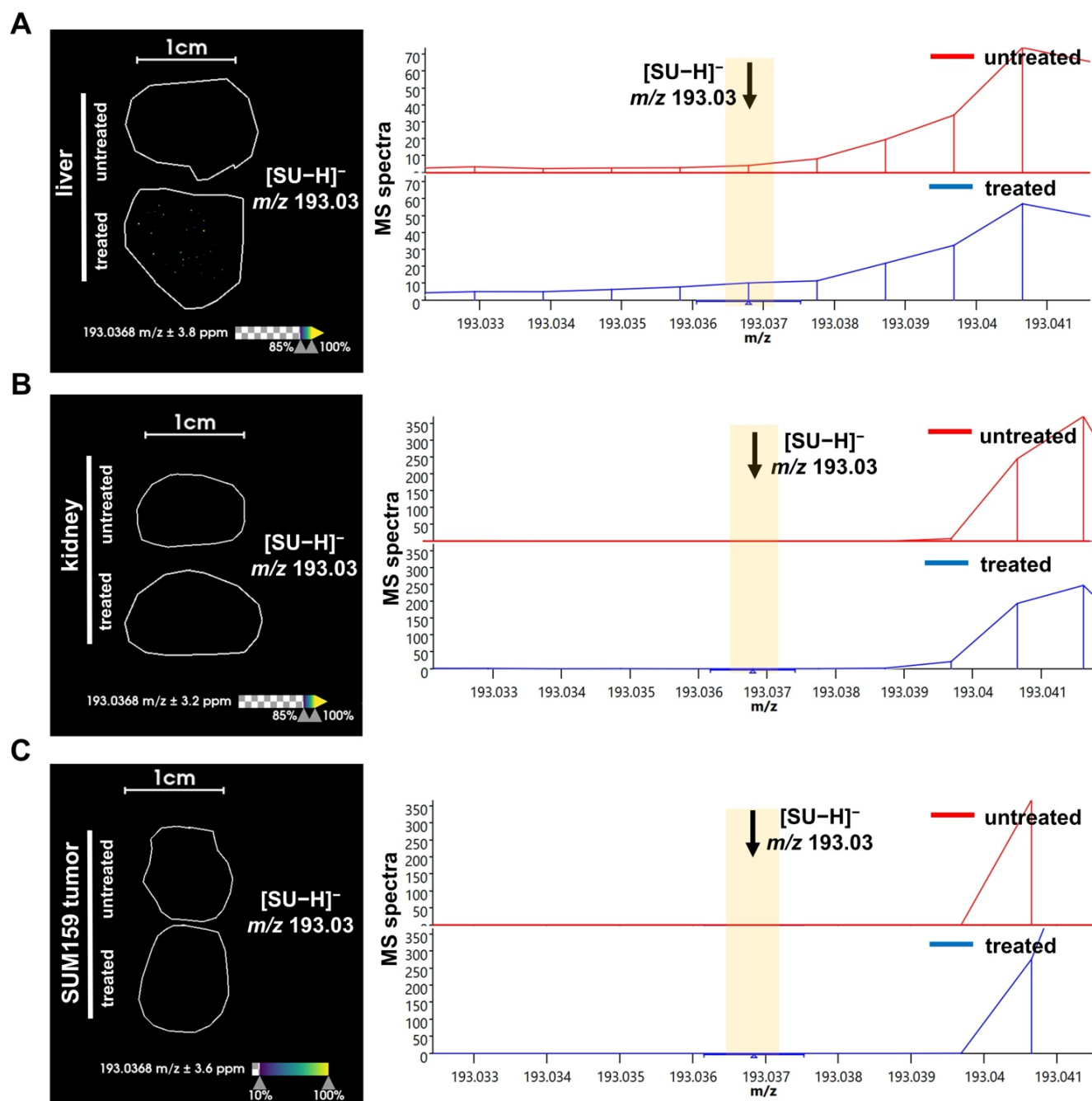


Figure S12. MALDI imaging of salicyluric acid (SU) distribution in tissue sections from aspirin treated versus untreated control mice. MALDI imaging and corresponding average spectra of SU distribution in representative (A) liver, (B) kidney, and (C) SUM159 tumor sections from 300 mM aspirin-treated (bottom, blue spectra) and untreated control (top, red spectra) mice. The data show that the $[M-H]^-$ ion of SU at m/z 193.03 Da was not detected in any tissues, neither in tissues from aspirin treated mice nor in those from untreated control mice. The MALDI images were acquired at 100 μ m pixel size in negative ion mode using a timsTOF fleX MALDI-2 instrument with norharmane matrix and PAA as an additive.

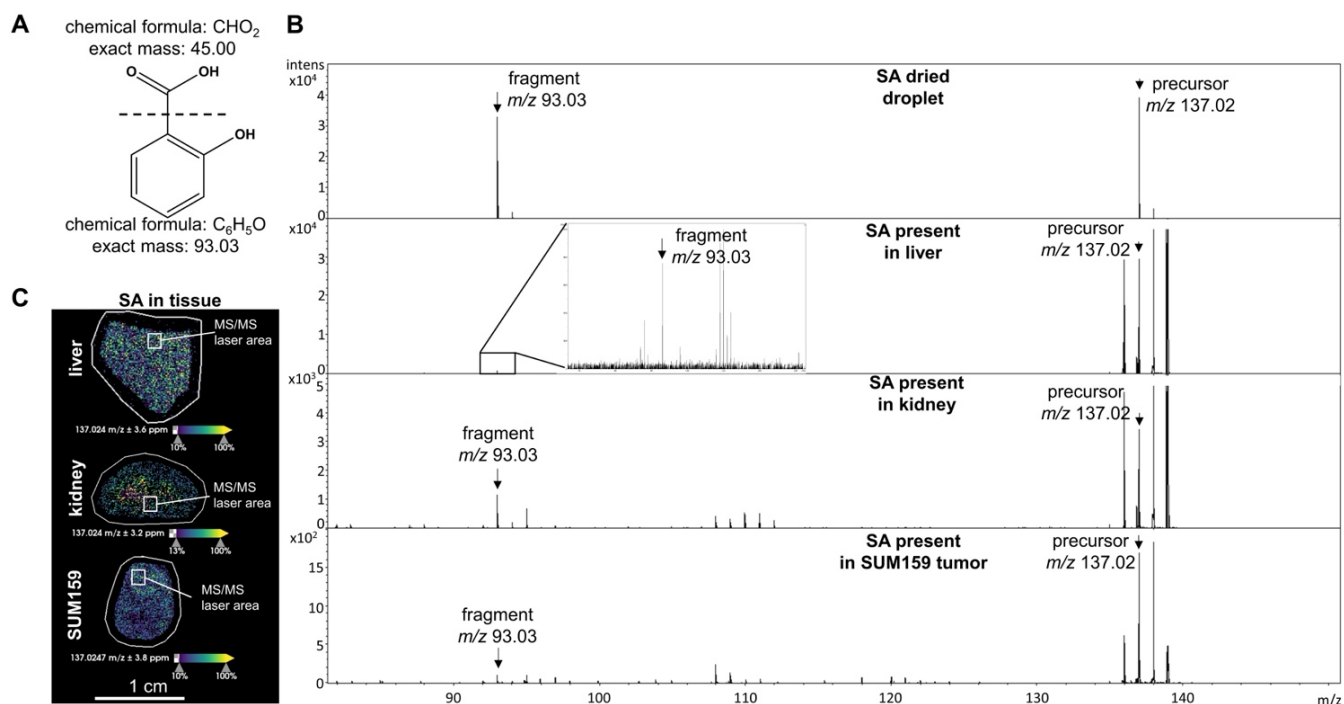


Figure S13. MS/MS spectra in negative ion mode for m/z 137.02, identified as SA. (A) The chemical structures of characteristic fragments are illustrated. (B) The precursor peak at m/z 137.02 Da and its fragment ion at m/z 93.03 Da are shown (top to bottom) from a dried SA droplet, and from liver, kidney, and SUM159 tumor sections. (C) The MS/MS laser area used for the analysis is highlighted with a white box.

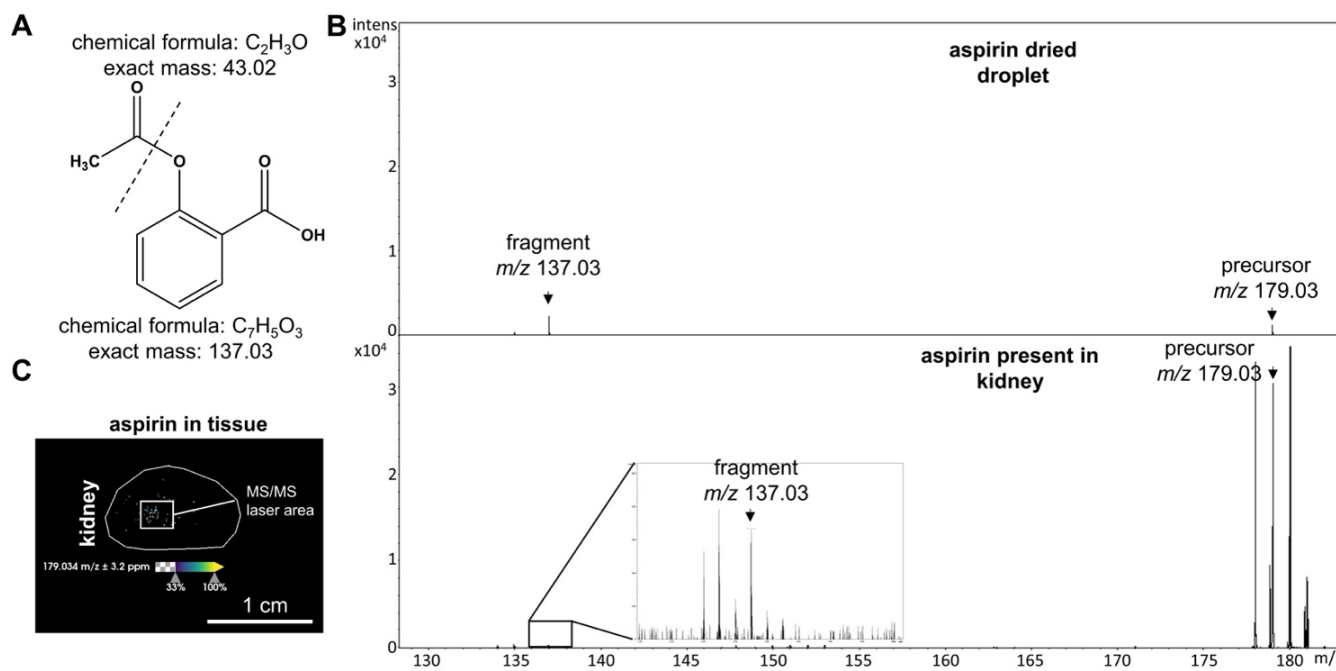


Figure S14. MS/MS spectra in negative ion mode for m/z 179.03, identified as aspirin. (A) The chemical structures of characteristic fragments are illustrated. (B) The precursor peak at m/z 179.03 Da and its fragment ion at m/z 137.03 Da are shown from a dried aspirin droplet (top) and in a kidney section (bottom). (C) The MS/MS laser area used for the analysis is highlighted with a white box.

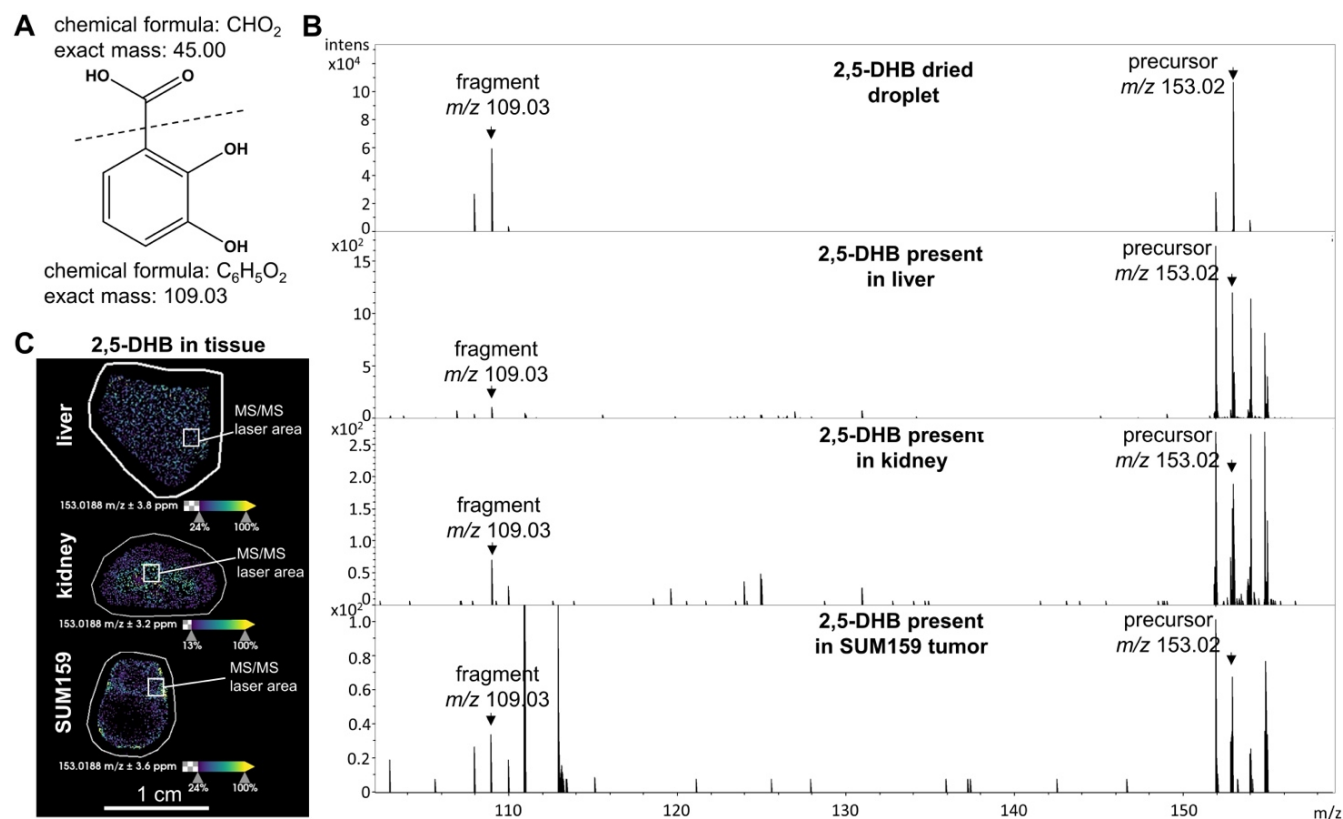


Figure S15. MS/MS spectra in negative ion mode for m/z 153.02, identified as 2,5-DHB. (A) The chemical structures of characteristic fragments are illustrated. (B) The precursor peak at m/z 153.02 Da and its fragment ion at m/z 109.03 Da are shown from a dried 2,5-DHB droplet, and from liver, kidney, and SUM159 tumor sections. (C) The MS/MS laser area used for the analysis is highlighted with a white box.

quantification methodology

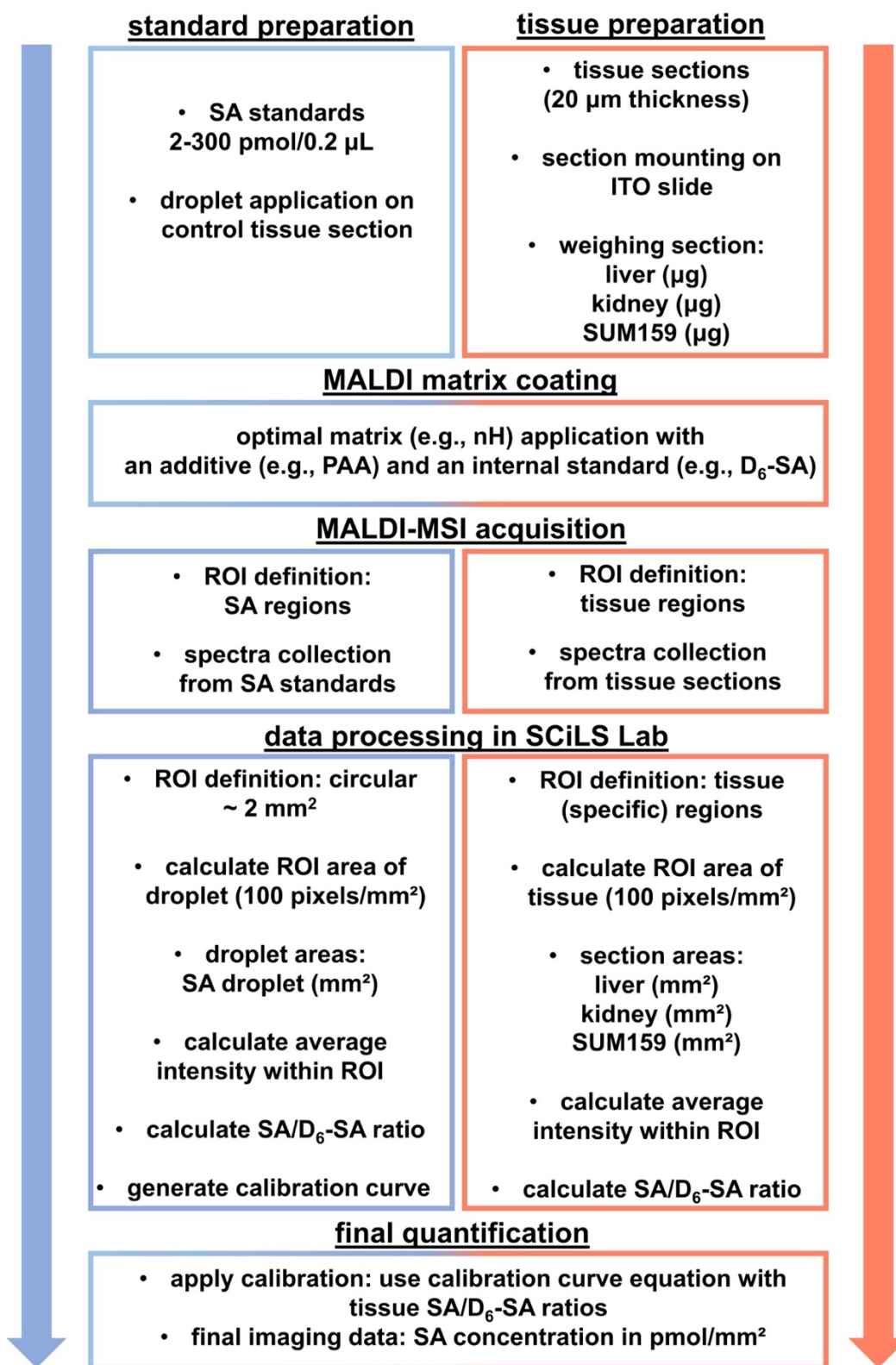


Figure S16. Comprehensive workflow map for SA quantification in tissue samples by QMALDI-MSI.

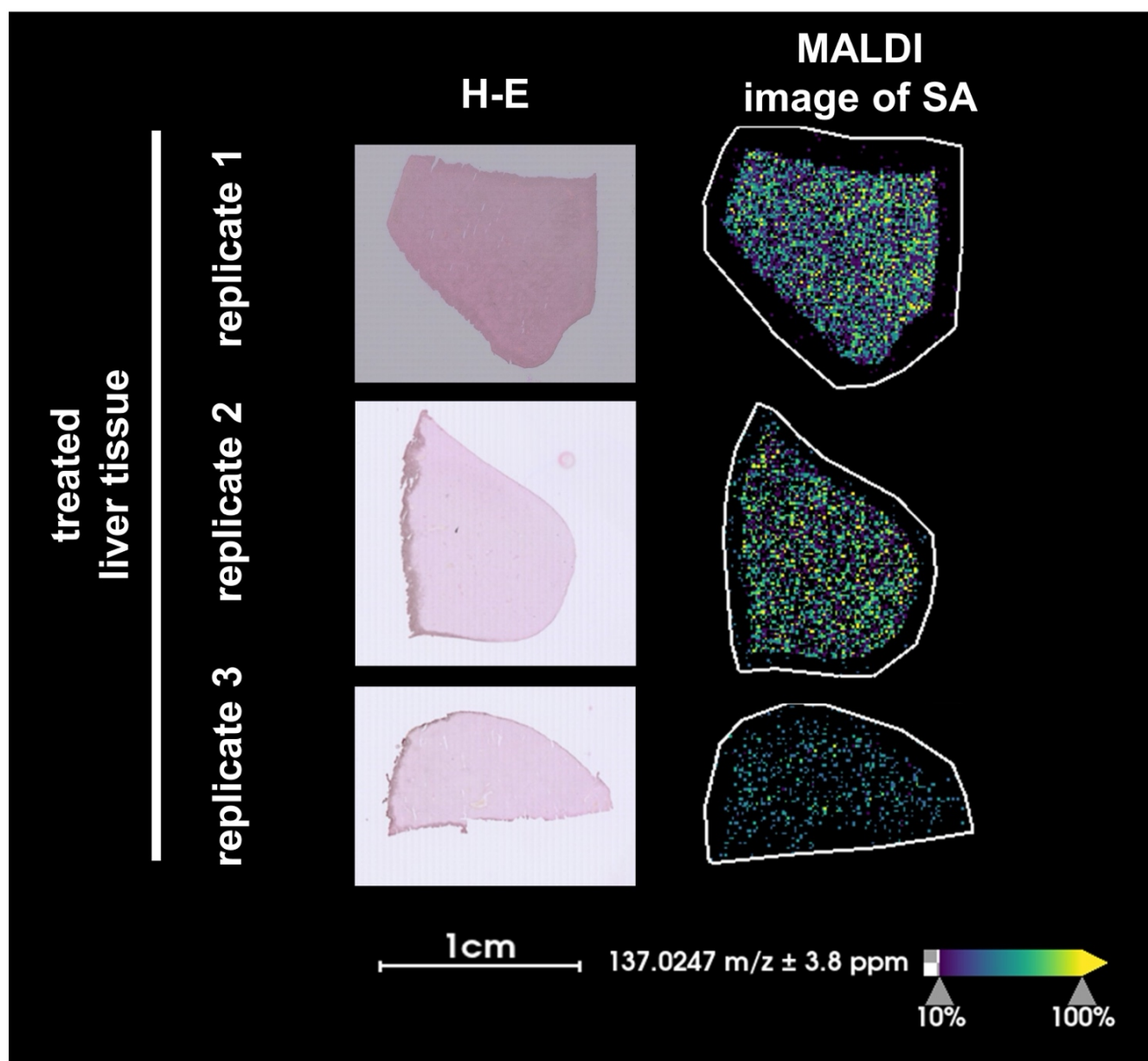


Figure S18. Microscopic images of liver sections stained with Hematoxylin-Eosin (H-E), alongside MALDI imaging. Microscopic images of H-E-stained liver sections from three biological replicates, accompanied by corresponding MALDI images showing the distribution of SA (m/z 137.02 Da, $[M-H]^-$) in liver tissue sections from aspirin treated mice. MALDI images were acquired using a timsTOF fleX MALDI-2 instrument with norharmane matrix and peracetic acid additive at 100 μm pixel size in negative ion mode.